Gadolinium for neutron detection in current nuclear instrumentation research: A review

Jonathan Dumazert, Romain Coulon, Quentin Lecomte, Guillaume H.V. Bertrand, Matthieu Hamel

▶ **To cite this version:**

Jonathan Dumazert, Romain Coulon, Quentin Lecomte, Guillaume H.V. Bertrand, Matthieu Hamel. Gadolinium for neutron detection in current nuclear instrumentation research: A review. Nuclear Instruments and Methods in Physics Research Section A: Accelerators, Spectrometers, Detectors and Associated Equipment, 2018, 882, pp.53 - 68. 10.1016/j.nima.2017.11.032 . cea-01765117

HAL Id: cea-01765117
https://cea.hal.science/cea-01765117

Submitted on 5 Jul 2023

HAL is a multi-disciplinary open access archive for the deposit and dissemination of scientific research documents, whether they are published or not. The documents may come from teaching and research institutions in France or abroad, or from public or private research centers.

L'archive ouverte pluridisciplinaire **HAL**, est destinée au dépôt et à la diffusion de documents scientifiques de niveau recherche, publiés ou non, émanant des établissements d'enseignement et de recherche français ou étrangers, des laboratoires publics ou privés.

Gadolinium for neutron detection in current nuclear instrumentation research: A review

Jonathan Nicolas Dumazert, Romain Coulon, Quentin Lecomte, Guillaume H. V. Bertrand, Matthieu Hamel

CEA, LIST, Laboratoire Capteurs Architectures Electroniques, 91191 Gif-sur-Yvette, France

Abstract

Natural gadolinium displays a number of remarkable physical properties: it is a rare earth element, composed of seven stable or quasi-stable isotopes, with an exceptionally high magnetization and a Curie point near room temperature. Its use in the field of nuclear instrumentation historically relates to its efficiency as a neutron poison in power reactors. Gadolinium is indeed the naturally occurring element with the highest interaction probability with neutrons at thermal energy, shared between Gd-157 (15.65%, 254000 b cross section) and Gd-155 (14.8%, 60900 b) isotopes. Considering that neutron capture results in an isotopic change, followed by a radiative rearrangement of nuclear and atomic structures, Gd may be embodied not merely as a neutron poison but as a neutron converter into a prompt photon and an electron source term. Depending on the nature and energy of the reaction products (from a few-keV Auger electrons up to 8 MeV gamma rays) that the detector aims at isolating as an indirect neutron signature, a variety of sensor media and counting methods have been introduced during the last decades. This review first draws a theoretical description of the radiative cascade following $Gd(\eta,\gamma)$ capture. The cascade may be subdivided into regions of interest, each corresponding to dedicated detection designs and optimizations whose current status is detailed. This inventory has allowed the authors to extract and benchmark key figures of merit for the definition of a detection scheme: neutron attenuation, neutron sensitivity (cps/nv), gamma rejection, neutron detection limit in a mixed field, intrinsic or extrinsic moderation, and transportability. On this basis, the authors have identified promising paths for Gd-based neutron detection in contemporary instrumentation.

Keywords

Neutron detection, Gadolinium, Compensation, Gas, Solid-state media

1. Introduction

Neutron detection and counting form a crucial and multidisciplinary issue in nuclear measurement. This review will have a special, although non restrictive focus on real-time detection and dosimetry for low-level neutron monitoring in the presence of a low-level gamma background [1]. Neutron radiation is, for instance, weakly attenuated by air and is deeply penetrating, which justifies the acute attention that it receives in radioprotection. Multiple environments require specific monitoring of neutron dose rate. For nuclear industry workers, these include fuel (U-235, Pu-239) fabrication and reprocessing units, power plants, and storage and decontamination sites for spent fuel [2]. The irradiation of staff (and patients) within the proximity of medical, research and industrial accelerators, as well as users of calibration neutron sources, is also strictly regulated [3]. Neutron counting plays a major role in passive, non-destructive control of fissile isotopes all along the fuel cycle, including inventory purposes, characterization of nuclear waste packaging and criticality monitoring [4]. Eventually, neutron detection is one of the keystones of special nuclear material (SNM: U-233, U-235, Pu) detection in the frame of nuclear and radiological threat prevention [5]. Neutron radiation portal monitors (RPMs) are installed in public places, critical entry checkpoints, and national borders, to prevent nuclear material proliferation and the risk of a "dirty bomb" contaminating an extended area.

Neutron radiation, as well as electromagnetic waves, belongs to the category of neutral radiations, *i.e.* as a neutron passes through matter, it is not affected by Coulomb forces from electrons in the medium. On the contrary, free neutrons interact with matter nuclei, by recoil or by nuclear reaction, leading to the emission of secondary charged particles that ionize the sensor and allow for a charge carrier-induced signal to be collected [6]. Neutron radiation is therefore qualified as indirectly ionizing and is

solely detected by the ionization signature from the charged products of neutron diffusions and reactions. Diffusions are only practically exploitable when the atomic mass of the target nucleus is close enough to that of one of the incident neutrons and when the kinetic energy T_n of the neutron falls into the fast range, usually defined between 1 and 10 MeV, essentially ^{1}H(n,n') diffusions [7]. Conversely, nuclear reactions of interest for neutron detection essentially take advantage of isotopes with interaction probability with neutron at thermal energy (i.e.$E_n = 25\ MeV$ at 19 °C) [6]. These are mainly ^{3}He(n,p), ^{10}B(n,α), ^{6}Li(n, α), ^{157}Gd(n,γ), ^{155}Gd(n,γ) and ^{113}Cd(n,γ) reactions. For these reactions to be put into play, it is therefore necessary that neutron radiation has been moderated before reaching the converter, either through diffusions inside the environment (for instance, the human body in the case of personal dosimeters) or by the traversing through a dedicated moderator set around the detection medium. Table 1 summarizes the key figures of merit (equivalent microscopic surface or cross section, liberated energy or Q-value, type of interaction products) for the main neutron–nucleus interactions used in nuclear instrumentation.

Helium-3 is the most commonly deployed converter in neutron counters found on the market. The inert He-3 gas under pressure is contained inside a tube, which is itself placed within a hydrogenous moderator whose dimensions maximize the neutron capture rate inside the gas. Charged particles, produced by the reaction (protium and tritium nuclei), directly ionize the gaseous medium, generating a cloud of charge carriers that induce the detected signal. Commercial detectors display a neutron sensitivity within the order of magnitude of one count per neutron nanosievert (1 c.nSv^{-1}) against a gamma vulnerability within the order of magnitude of 10^{-3} c.nSv^{-1}, hence obtaining a n/γ discrimination ratio of 10^{-3}, which is robust up to 1 mSv.h^{-1} gamma dose rates [8]. It is thus the combination of He-3 high thermal neutron sensitivity (explained by the 5330 b cross section from Table 1) and gamma rejection of the gaseous medium that makes such detectors a reference. However, 9/11 attacks have led to the deployment of a rising quantity of SNM monitors at borders, causing the He-3 demand to skyrocket [9]. The shadow of a worldwide shortage and the strategic stakes related to the He-3 resource (United States and Russian stocks of nuclear weapons being the main providers of the isotope during the 2000 decade) have severely affected the cost of the detectors [10]. The quest for alternative technologies to He-3 proportional counters has therefore become a prominent topic of research in contemporary nuclear instrumentation.

Interaction	**Energy T_n**	**Cross section (b)**	**Q-value (MeV)**	**Products**
^{1}H (n,n')	**100 keV – 10 MeV**	**0.7–28**	–	**proton**
^{3}He (n,p)	Thermal	5330	0.764	proton, triton
^{10}B (n,α)	Thermal	3840	2.792	alpha, lithium ion
^{6}Li (n,α)	Thermal	940	4.78	alpha, triton
^{137}Gd (n,γ)	Thermal	254000	7.937	photons, electrons
^{155}Gd (n,γ)	Thermal	60900	8.536	photons, electrons
^{113}Cd (n,γ)	Thermal	20600	9.04	photons, electrons

Table 1. Interactions of interest for neutron detection and counting.

2. Key physical features, supply data and instrumental uses of gadolinium

2.1. General physical properties of Gd

Gadolinium is naturally present as a combination of five stable and two quasi-stable isotopes, all labeled $^{A}_{64}\mathrm{Gd}$ with Z = 64 being the atomic number and A the mass number of the isotope: $^{152}_{64}\mathrm{Gd}\ (T_{1/2} = 1.08\,.\,10^{14}\ a;\alpha)$, $^{154}_{64}\mathrm{Gd}$, $^{155}_{64}\mathrm{Gd}$, $^{157}_{64}\mathrm{Gd}$ and $^{160}_{64}\mathrm{Gd}\ (T_{1/2} > 10^{21}\ y;\beta^{-1}\ \beta^{-1})$. Its

average atomic mass equals 157.25 ± 0,03 u [11]. The electrons of a Gd atom cloud populate successive electronic layers with respect to the value of their principal quantum number *n*, according to the formula $(K)^2\ (L)^8\ (M)^{18}\ (O)^9\ (P)^2$. Taking into account all four quantum numbers, the electronic configuration of Gd reads

$$[Gd]=1s^2\ 2s^2\ 2p^6\ 3s^2\ 3p^6\ 3d^{10}\ 4s^2\ 4p^6\ 4d^{10}\ \mathbf{4f^7}\ 5s^2\ 5p^6\ 5d^1\ 6s^2 \qquad (1)$$

From these considerations, it follows that Gd is part of the 6th period and 4f-subblock of the periodic table. Gadolinium is classified among the lanthanide series, comprising all elements with atomic numbers ranging from Z = 57 (La) up to Z = 71 (Lu), chemically similar to lanthanum. For a lanthanide element, including Gd, the +3 oxidation state is the most stable. As a result, Gd is found in natural form and in the majority of synthetic compounds as a Gd^{3+} trivalent cation, while it may be obtained as a Gd^{2+} divalent cation in solutions [12]. Gadolinium also finds its place among the metal group of rare earth elements, in which Sc (Z =21) and Y (Z = 39) are added to the lanthanide series. Because of analog chemical properties, these elements are found as a mixture in a limited number of minerals, such as monazite and bastnaesite [13].

Gadolinium, when incorporated in low amounts (of the order of 1 wt%) in iron and chromium alloys, has the property to improve the workability, mechanical resistance, and high-temperature resistance to oxidation of the material [14]. Together with Fe, Co, and Ni, Gd is reported as one of the four simple ferromagnetic elements, although the notion is debated [15]: it remains that Gd presents an exceptionally high magnetization field and unusually low Curie temperature T_c, marking the transition from a state of intrinsic magnetic order to the paramagnetic state of the metal. The magnetization of Gd according to the direction of an external magnetic field then admits an inflexion point within the vicinity
$289\ K \leq T_c \leq 293\ K$ [[16], [17]], so that the ferromagnetic–paramagnetic phase transition of Gd may be embodied as a room-temperature heat flux sensor [18].

2.2. Supply data (2007–2017)

Gadolinium is never found in its raw form as a natural material. The ionic radius of the Gd^{3+}cation equals 107.8 pm, which explains why the crystal structures of monazite and bastnaesite are favorable to Gd inclusions. Active mining fields dedicated to the extraction of these ores may be found in China (Bayan Obo) or Australia (Mount Weld) [19]. The process of Gd purification comprises several key steps: extraction, mineral processing (grinding and concentration of ores by floatation), chemical processing (obtention of Gd hydroxides, chlorides and carbonates under acidic or basic attacks), and elementary separation. Before this last stage, Gd purity reaches 90%, expressed as a percentage of the total content in rare earth oxides. The separation step allows for an elevation of purity from 90% to 99% or even 99.99%, depending on the technique used. The continuous separation process by solvent-based extraction allows for a purification above 99.99%. The purification method of Gd directly affects the cost of the raw material. The obtention of metal Gd may be achieved by metallothermal reduction of Gd fluoride [20] according to the reaction equation

$$2\ GdF_3 + 3\ Ca \rightarrow 2\ Gd + 3\ CaF_2 \qquad (2)$$

For the sake of this introduction, we provide an overview of the evolution of metal Gd cost over the last decade. We have superimposed in Fig. 1 the evolution, between 2007 and 2016, of 99%-pure metal Gd [20] with the most commonly used neutron converter in the detection market, He-3 [10]. The selling price of Gd (hereby expressed in United States Dollar per Liter, US$/L) is easily accessible in literature, contrary to the cost of He-3 or tritium (^3_1H disintegrates into ^3_2He by β^- -decay). This difficulty reflects the criticality of the He-3 resource. As previously mentioned, He-3 production is essentially a by-product of nuclear weapon maintenance [21]. As a consequence, the uncertainties attached to the cost of He-3 are high, and not only depend on the nuclear reactor but also on the breeder system [22].

The cost of Gd is currently trending downwards and is approximately 30 times lower than the cost of He-3. From the available supply data, we are therefore able to state that Gd is both significantly cheaper and less critical than He-3, corroborating its interest as an alternative base for neutron detection technologies.

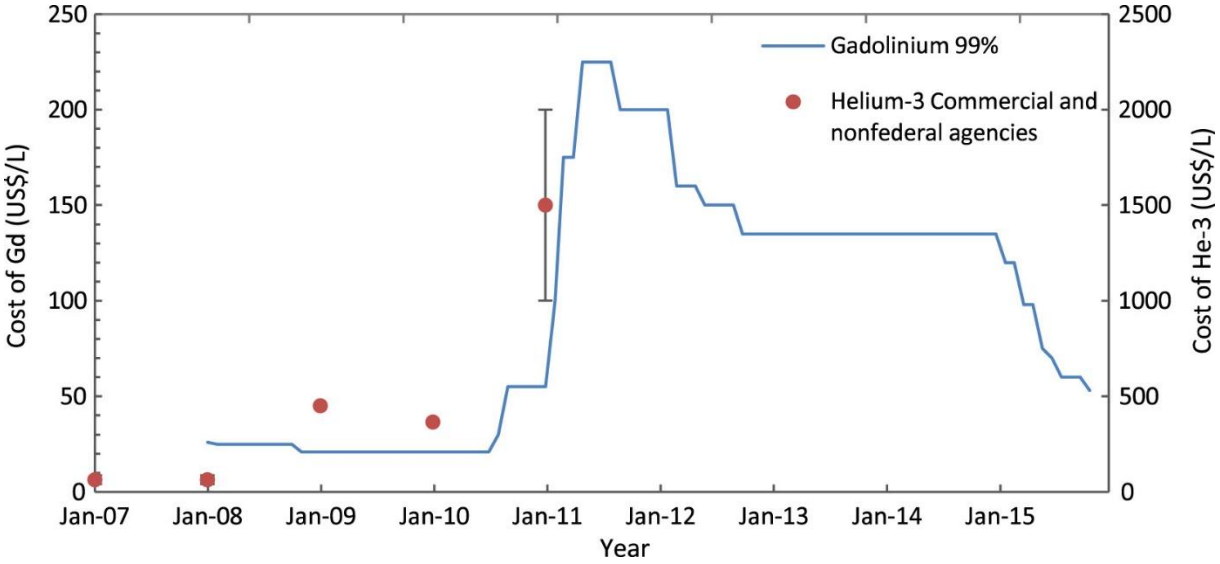

Fig. 1. Evolution of 99% Gd and He-3 costs between 2007 and 2016.

2.3. Traditional use of Gd in nuclear instrumentation

The use of Gd in the field of neutronics historically relates to its efficiency as a neutron poison. The energy distribution of the neutron capture cross section $\sigma_{Gd(n,\gamma)}$ (E_n) is reproduced in Fig. 2, according to the interpolated data compiled in the IRDFF-1.0 database, published by the International Nuclear Data Committee (INDC) [23]. The characteristic clearly shows a thermal-energy cut-off, the value of $\sigma_{Gd(n,\gamma)}$ (E_n) falling from $\sigma_{Gd(n,\gamma)}$ =8690 b down to $\sigma_{Gd(n,\gamma)}$ =833 b (*i.e.* more than one decade reduction) between E_n = 100 meV and E_n = 1250 meV (epithermal range). This abrupt distribution explains why the use of Gd as a neutron absorber is limited to slow neutron environments, typically to capture neutrons at thermal energy.

From the values plotted in Fig. 2, it can be deduced that Gd is the stable, naturally occurring element with the highest interaction probability with neutrons at 25 meV. Table 2, which is built from the data provided by the IAEA Prompt Gamma-Ray Neutron Activation Analysis base (PGNAA) [24], presents the absolute cross section σ_A associated with every ${}^{A}_{64}\mathrm{Gd}$ isotope for thermal neutron capture. It also contains the cross sections $\sigma_{A,w}$ weighted by the atomic fraction P_A of the ${}^{A}_{64}\mathrm{Gd}$ isotope in natural Gd. The resulting cross section of natural Gd is given by $\sigma = \sum_A \sigma_{A,w} = 48800 \pm 150$ b, with 99.99% due to Gd-157 (254 kb) and Gd-155 (60.9 kb). Natural Gd, considered from the perspective of the interaction with thermal neutrons, may therefore by simplified as a two-absorbing isotope system:

$$\sigma = 48800\ \mathrm{b}\ ;\ \left\{\left({}^{157}_{64}\mathrm{Gd}, 81.5\ \%\right); \left({}^{155}_{64}\mathrm{Gd}, 18.5\ \%\right)\right\} \qquad (3)$$

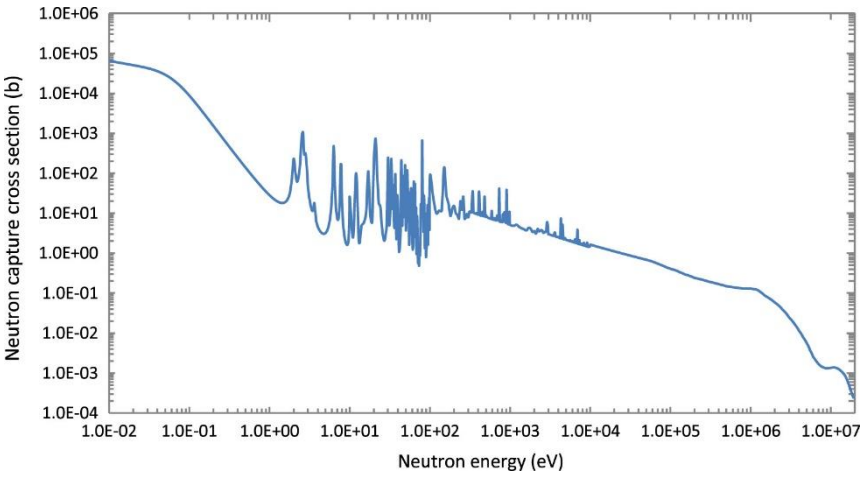

Fig. 2. Capture cross section as a function of neutron energy for natural Gd (IRDFF-1.0).

Elements with a high cross section for thermal neutron capture (Gd, Cd) find a straightforward application in the context of reactor instrumentation and control. Fixed, burnable Gd_2O_3 poisons are loaded into the core to control excess fuel reactivity after restart phases [25], either as a separate pin lattice [26] or, more commonly, directly mixed with UO_2 inside the fuel rod [27]. Integrated Gd poisons, although they necessitate a specific preparation of nuclear fuel and tend to degrade rod thermal conductivity, are easier to reprocess and do not raise moderation issues. The content of Gd in poisoned rods varies between 7% and 9% and these gadoliniated rods may be found in quantities varying from 8 to 20 in Pressure Water Reactor fuel assemblies. As burnable poisons also serve the purpose of shaping the neutron flux spatial distribution, they are usually placed near the center of the core. As a powerful neutron absorber, Gd enters into the composition of neutron shielding alloys, such as Ni–Cr–Mo–Gd [28], for nuclear reactor safety and fissile material storage [29]. Another notable utilization of the large Gd thermal neutron capture cross section is water-soluble, inorganic Gd(III) nitrate poisons with complete formula: $(Gd(NO_3)_3 . 6H_2O)$. Such Gd-based poisons have notably been used as a part of emergency shutdown systems in heavy water nuclear reactors [30].

Isotope ${}^{A}_{64}\mathrm{Gd}$	**Atomic fraction** P_A (%)	$\sigma_A\,(b)$	$\sigma_{A,w}\,(b)$
${}^{152}_{64}\mathrm{Gd}$	0.2 ± 0.01	735 ± 20	1.47 ± 0.04
${}^{154}_{64}\mathrm{Gd}$	2.18 ± 0.03	85 ± 12	1.85 ±0.26
${}^{155}_{64}\mathrm{Gd}$	14.80 ± 0.12	30900 ± 500	9013 ± 74
${}^{156}_{64}\mathrm{Gd}$	20.47 ± 0.13	2.4 ± 0.2	0.49 ± 0.04
${}^{157}_{64}\mathrm{Gd}$	15.65 ± 0.02	254000 ± 800	39751 ± 125
${}^{158}_{64}\mathrm{Gd}$	24.84 ± 0.07	2.2 ± 0.2	0.55 ± 0.05
${}^{160}_{64}\mathrm{Gd}$	21.86 ± 0.19	1.4 ± 0.3	0.31 ± 0.07

Table 2. Absolute and weighted isotopic cross sections for thermal neutron capture (PGNAA).

3. Thermal neutron radiative capture by Gd-155 and Gd-157 nuclei

3.1. Isotopic change and Q-value in 155Gd (n,γ) and 157Gd (n,γ) reactions

Neutron capture by a Gd-155 or Gd-157 results in an isotopic change of the nucleus, from one stable to another stable isotope, as described in reaction Eqs.(4), (5) :

$${}^{155}_{64}\mathrm{Gd} + {}^{1}_{0}\mathrm{n} \rightarrow {}^{156}_{64}\mathrm{Gd}^{*} \rightarrow {}^{156}_{64}\mathrm{Gd} + RP \qquad (4),$$

$${}^{157}_{64}\mathrm{Gd} + {}^{1}_{0}\mathrm{n} \rightarrow {}^{158}_{64}\mathrm{Gd}^{*} \rightarrow {}^{158}_{64}\mathrm{Gd} + RP \qquad (5)$$

where the reaction products, produced by a radiative rearrangement of nuclear and atomic structures, have been labeled *RP*.

In addition to being high-cross section interactions, nuclear reactions in Eqs. (4) and (5) are strongly exothermic, with a Q-value of $Q_{155} = 8536.35 \pm 0.07$ keV and $Q_{157} = 7937.39 \pm 0.06$ keV respectively [31]. After weighting by the coefficients quoted in paragraph 2.3, a Q-value per neutron capture in natural Gd is derived: Q = 8048.2 ± 0.6 keV. This resulting energy is shared between all reaction products, which are freed as excited nuclei ${}^{156}\mathrm{Gd}^{*}$and ${}^{158}\mathrm{Gd}^{*}$and regain their fundamental energy level, i.e. their quantum state of lowest energy.

A 49-kb microscopic cross section and 8 MeV Q-value form two exceptionally favorable figures of merit for thermal neutron detection [32], as would highlight a comparison between features in Table 1. It follows that Gd may be embodied not merely as a neutron poison but as a neutron converter into a prompt, secondary source term, represented by the sum of *RP*, which is subdivided itself into a prompt photon and a prompt electron source term. However, the *RP* term is dominated by electromagnetic radiations [33] which are likely to escape from most detection media and have the same nature as the

natural gamma radioactivity they need to be discriminated from. The exploitability of ^{155} Gd (n,γ) and ^{157} Gd (n,γ) reactions in neutron detection therefore depends on the typology and energy distribution of *RP*, as will be discussed in the rest of this section.

3.2. Continuous Gd (n,γ) signature: Prompt gamma-ray continuum between 0 and *Q*

Gadolinium nuclei, after neutron capture, are found within a discrete set of energy levels, each of them being characterized by angular momentum *J*, parity *P* (with notation J^P) and isospin *T*. The return of ^{156}Gd*and ^{158}Gd*nuclei to ground state is promptly mediated by the emission of gamma rays. The de-excitation gamma-ray spectrum for both isotopes is modeled as the superimposition [33] of:

- A *continuous component*, lying between 0 and the Q-value, whose probability density function reaches a maximum of about 10^{-2} nc^{-1} (per neutron capture) in the vicinity of 2 MeV ;
- A *discrete component*, whose lines correspond to possible differences between allowed energy levels.

Different probabilistic, Monte Carlo codes are available for particle transport modeling, among which MCNP is a reference tool for neutron diffusions and captures [34]. The MCNP6 program simulates a complete history of every generated corpuscle, for both source terms and recoil products, until kinetic energy falls below an adjustable threshold [35]. A number of nuclear data libraries are available in addition to the MCNP6 code so that the gamma-ray *RP* of ^{157} Gd (n,γ) and ^{155} Gd (n,γ) reactions may be generated. The ENDF/B-VII.0 library is notably used to generate the prompt electromagnetic source term after neutron capture [36]. To obtain a representation of the photon spectrum generated by the library, a simple configuration was simulated: a neutron source with energy E_n = 25 meV was positioned at the center of a natural Gd ball, with isotopic composition from Table 2, density ρ = 7.901 g. cm^{-3}, and radius r = 10 µm. By using tally 4 (volumic particle fluence), with addition of SD4 (normalization) and E4 (energy distribution) options, the spectral distribution of photons exiting the Gd ball and crossing a surrounding, empty sphere with radius R = 1 cm per generated neutron (n^{-1}) is estimated. For this configuration, 88.67% of generated neutrons are captured by Gd nuclei, and 99.84% of the photons, generated after captures, escape for Gd, so that the output photon fluence reliably illustrates the library source term. The obtained spectral distribution, with respective contributions from Gd-155 and Gd-157 isotopes, is reproduced in Fig. 3.

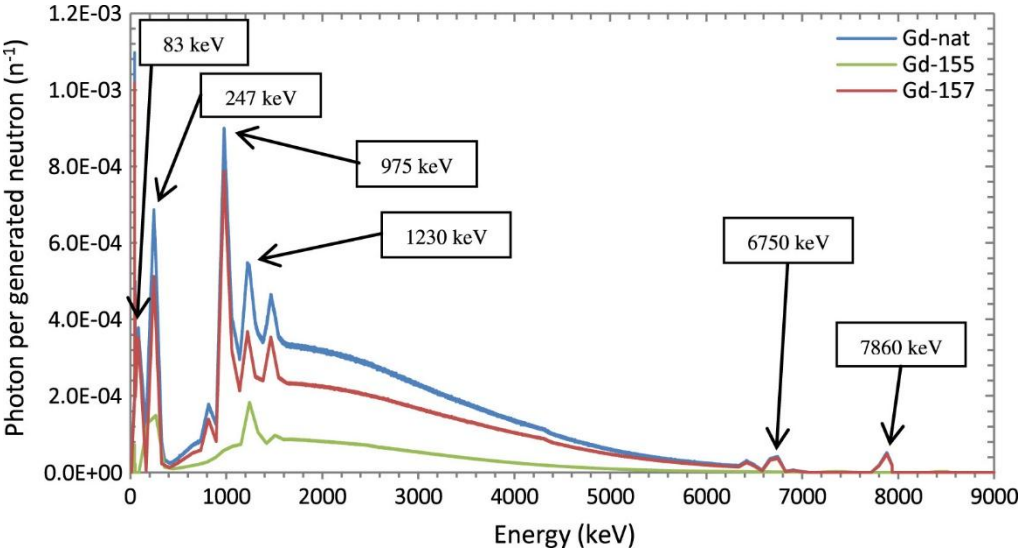

Fig. 3. Photon spectrum exiting a 10-µm-radius Gd ball per generated thermal neutron (MCNP6, ENDF/B-VII.0 library).

The source term from the library carries the continuous, gamma-ray component of *RP*: for instance, energy 7.86 ± 0.05 MeV, *i.e.* 99.0 ± 0.1% of Q-value Q_{157} ~7.94 MeV expected for a ^{157} Gd (n,γ) capture reaction. This results stands in excellent agreement with the findings of, Sakurai et al., who

stated that, after ^{157} Gd (n,γ) capture, 99.2% of the Q-value is carried by photon products of the reaction (the rest, 0.8% of the Q-value, being shared by low-energy electrons, as discussed below).

Simulation efforts have also been conducted in GEANT4 to model Gd (n,γ) gamma emission. Two implementations of the de-excitation source term are available in standard GEANT4, with respective merits and domains of validity. The "Final State Model", based on Neutron Data Library (G4NDL), is found to represent more adequately individual gamma line values, whose description will be given in the following paragraph, but does not preserve the Q-values quoted in paragraph 3.2 [37]. Conversely, the "Photon Evaporation Model" carries more adequately the Q-value of Gd (n,γ) reactions, although to the detriment of individual line intensities and gamma-ray multiplicity [[37], [38]]. The selection of a model should then be driven by the figures of interest in a given detection scheme. Typically, large detectors as those described in Section 6, rely on a high energy deposition (above 2 MeV) from Gd capture gamma rays, so that their design should be based on an accurate estimation of the released Q-value and therefore the Photon Evaporation Model. In the framework of the Double Chooz Experiment, a modified, dedicated model was developed by adding individual lines to a continuum, computed on the basis of an enhanced generalized Lorentzian distribution, and adjusting the result to experimental [39].

3.3. Discrete Gd (n,γ) signature: Prompt gamma rays, internal conversion electrons, X rays and Auger electrons

3.3.1. Discrete gamma-ray spectrum

Although the majority of Q-values in ^{155}Gd (n,γ) and ^{157}Gd (n,γ) reaction is carried by the prompt gamma-ray continuum, the discrete signature of these reactions is essential in many identification schemes, each of them focusing on a set of privileged rays. The *Prompt Gamma-Ray Neutron Activation Analysis* (PGNAA), made available by the International Atomic Energy Agency (IAEA), is built from isotopic data compiled in the Evaluated Nuclear Structure Data File and updated from measurements on the nuclear research reactor in Budapest [40]. PGNAA draws up the inventory of discrete, prompt gamma rays following neutron captures by Gd-157 and Gd-155 nuclei. The spectrum comprises 390 rays between 79.51 and 7857.67 keV from the Gd-157 isotope, and 324 rays between 57.592 and 6764.83 keV for Gd-155. The emission rate $P(E_\gamma)$per neutron capture (nc^{-1}) is calculated from the emission cross-section, noted $\sigma_\gamma^A(E_\gamma)$, of a given isotope for a gamma ray of energy , the total reaction cross-section σ_0 of the isotope with thermal neutrons and the abundance ω_A of the isotope in the natural element, according to:

$$P(E_\gamma) = \frac{\sigma_\gamma^A(E_\gamma)}{\sigma_0 . \omega_A} \qquad (6)$$

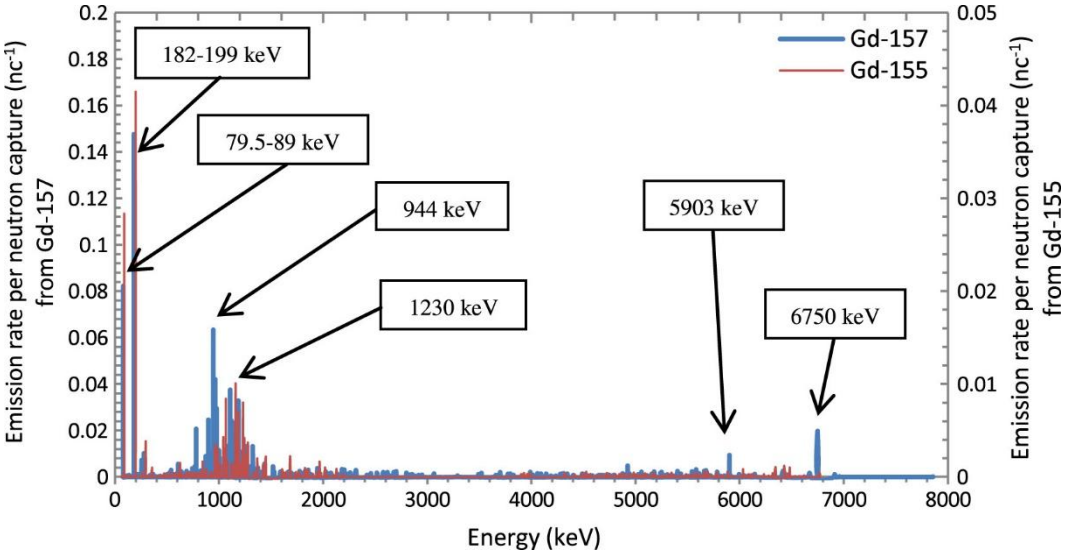

Fig. 4. Weighted discrete prompt gamma-ray spectrum after Gd (n,γ) capture (IAEA).

The discrete spectrum, with the emission rate per Gd (n,γ) capture in the vertical axis, on the left from the Gd-157 isotope and on the right the Gd-155 isotope, is presented in Fig. 4. The distribution is notably dominated by two low-energy doublets,

$\gamma_{1,157}\left(E_{\gamma_{1,157}} = 79.51\ \text{keV}\right)$ and $\gamma_{2,,157}\left(E_{\gamma_{2,157}} = 181.931\ \text{keV}\right)$ from Gd-157, and $\gamma_{1,155}\left(E_{\gamma_{1,155}} = 88.967\ \text{keV}\right)$ and $\gamma_{2,155}\left(E_{\gamma_{2,155}} = 199.213\ \text{keV}\right)$ from Gd-155. These energies correspond to transitions from the first excited state 2+ to the fundamental state 0+ for the $\gamma_{1,j}$ set, and from the second excited state 4+ to 2+ for the $\gamma_{2,j}$ set, as illustrated in Fig. 5 [[41], [42]].

The intensity of the mentioned gamma-ray doublets allows for a benchmark between reference works. Gräfe *et al.* [43] quote for both most intense rays following ^{157} Gd (n,γ) capture, *i.e.* E_γ = 79.51 keV and E_γ = 181.931 keV, and gamma emission rates

P(79.51 keV) = 0.098 ± 0.007 nc^{-1} and

P(181.931 keV) = 0.183 ± 0.017 nc^{-1}.

These values are compatible within one standard deviation with the emission rates (before isotopic correction)

P(79.51 keV) = 0.10 ± 0.01 nc^{-1} and

P(181.931 keV) = 0.18 ± 0.01 nc^{-1} ,

derived using Eq. (6). The hereby computed values are also within the same order of magnitude as the experimental values estimated by Sakurai et al. [33], equaling

P(79.51 keV) =0.115 nc^{-1} and P(181.931 keV) =0.136 nc^{-1}.

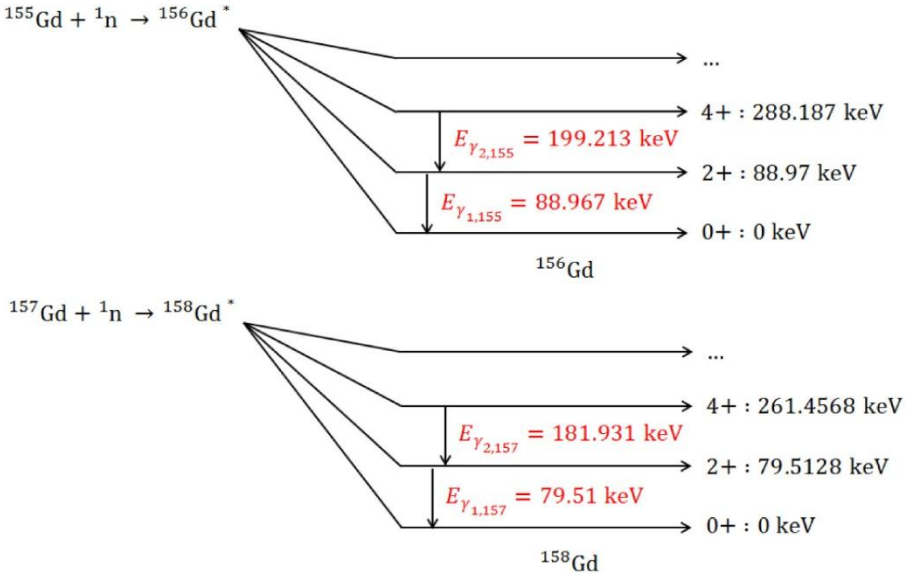

Fig. 5. First excited states of Gd-156 and Gd-158 nuclei and associated gamma transitions.

3.3.2. Internal conversion electrons

Prompt gamma emission is in competition with a nuclear de-excitation mode called *internal conversion*: a cloud electron directly acquires a fraction of the nucleus excitation energy and is expelled from the atom. As the wave function of cloud electrons is never null inside the atomic nucleus, there is indeed a probability of direct interaction between electrons and nucleons. The de-excitation series associated with 4+ to 2+ and 2+ to 0+ levels have been reported to be responsible for 96.7% of the energy carried by internal conversion electrons after ^{157}Gd (n,γ) capture [44], and similarly for ^{155} Gd(n,γ) capture [45].

The binding energy of an electron occupying the subshell is labeled $E_{li,m}$. Table 3 summarizes the binding energies [46] associated with the main electronic subshells implicated in the generation of internal conversion electrons.

Subshell m	K	L_1	L_2	L_3	M_1	M_2	M_3	M_4	M_5	N_1	N_2	O_1	O_2
$E_{li,m}$ (keV)	50.24	8.38	7.93	7.24	1.89	1.69	1.55	1.22	1.19	0.38	0.27	0.04	0.03

Table 3. Binding energies on K, L and M gadolinium shells.

For each of the four $\gamma_{i,j}, i \in \{1;2\}, j \in \{157;155\}$ transitions, introduced in paragraph 3.3.1 and every *m* electronic subshell, we label $C\ I\ e^-_{i,j,m}$ as the internal conversion electron expelled instead of gamma-ray emission. The emission yield for an internal conversion electron from *m* the subshell is noted $\eta_{C\ I\ e^-_{i,j,m}}$; we also define, for every transition, an internal conversion coefficient $\alpha_{i,j}$ according to

$$\forall i \in \{1;2\}, \forall j \in \{155;157\}, \alpha_{i,j} = \sum_m \eta_{C\ I\ e^-_{i,j,m}} \quad (7)$$

The internal conversion electron $E_{C\ I\ e^-_{i,j,m}}$ is given by the underlying gamma-ray transition $E_{\gamma_{i,j}}$ and the electron binding energy $E_{bi,m}$:

$$\forall i \in \{1;2\}, \forall j \in \{155;157\}, \forall m \in \{K; L_1; L_2; L_3; M_1; M_2; M_3; M_4; M_5\}, E_{C\ I\ e^-_{i,j,m}} = E_{\gamma_{i,j}} - E_{bi,m} \quad (8)$$

Table 4 presents the internal conversion yields computed by BrIccS v2.3 program [47], made available by the National Nuclear Data Center. The results stand in excellent agreement with the values reported in literature: Rösel et al. [48], for instance, derived conversion yields $\eta_{CIe^-_{1,157,K}} = 1.54$ and $\eta_{CIe^-_{1,155,K}} = 2.00$, compared to $\eta_{CIe^-_{1,157,K}} = 1.559$ and $\eta_{CIe^-_{1,155,K}} = 2.017$ in our calculation. From gamma emission rates and internal conversion yields, the emission rates Gd (n,γ) per capture for the main internal conversion electrons are eventually obtained.

j =157		*j* =155		
i = 1	*i* = 2	*i* = 1	*i* = 2	***m***
$\eta_{CIe^-_{1,157,K}}$ =2.017	$\eta_{CIe^-_{2,157,K}}$ =2.06.10-1	$\eta_{CIe^-_{1,155,K}}$ =1.559	$\eta_{CIe^-_{2,155,K}}$ =1.565.10-1	**K**
$\eta_{CIe^-_{1,157,K}}$ =3.021	$\eta_{CIe^-_{2,157,K}}$ =7.693.10-2	$\eta_{CIe^-_{1,155,K}}$=1.789	$\eta_{CIe^-_{2,155,K}}$ =5.31.10-2	**L**
$\eta_{CIe^-_{1,157,K}}$ =7.144.10-1	$\eta_{CIe^-_{2,157,K}}$ =1.78.10-2	$\eta_{CIe^-_{1,155,K}}$ =4.225.10-1	$\eta_{CIe^-_{2,155,K}}$ =1.24.10-2	**M**
$\alpha_{1,157}$ = 5.933	$\alpha_{2,157}$ =3.053.10-1	$\alpha_{1,155}$ =3.877	$\alpha_{2,155}$ =2.25.10-1	

Table 4. Internal conversion yields per electron shell (BrIccs)

3.3.3. X rays and Auger electrons

An internal conversion electron expelled from the *m* subshell leaves a vacancy, which is then filled by an electron from another subshell labeled *p* (necessarily $p > m$). The transition is mediated by the emission of electromagnetic radiation called *X rays*, whose energy is equal to the difference between binding energies:

$$\forall (m,p), E_{RX} = E_{bi,m} - E_{bi,p} \quad (9)$$

An alternative atomic de-excitation mode is represented by the emission of an electron from a subshell *n* located between *m* and *p* ($m < n < p$). Such a radiation is called *Auger electron* and carries energy equal to the transition energy minus its own binding energy:

$$E_{Ae^-} = E_{RX} - E_{bi,n} \quad (10)$$

Following one internal conversion of the K-shell with yield $\eta_{CIe^-_{i,j,K}}$, for instance, X rays and Auger electrons are radiated in the 30–50 keV range, with these major lines:

- K_{α_1}- X ray with energy $E_{K_{\alpha_1}} = 43.0$ keV (transition from L_3 to K) ;
- K_{α_2} - X ray with energy $E_{K_{\alpha_2}} = 42.3$ keV (transition from L_2 to K) ;
- K_{β_1} - X ray with energy $E_{K_{\beta_1}} = 48.7$ keV (average transition from M to K) ;
- K_{β_2} - X ray with energy $E_{K_2} = 50.0$ keV (average transition from N and O to K) ;
- Ke^- - Auger electron with energy $E_{Ke^-} = 34.9$ keV, *i.e.* the mean K_α emission energy minus the mean binding energy of L-shell electrons.

Relative intensities of X rays are tabulated [49], and Auger yield for Ke^- is reported to lie between 10% and 15% [50]; the representative emission rates per K-shell electron internal conversion are computed and tabulated in Table 4. Our results are also compatible with those reported in literature: Abdushukurov [51], for instance, quotes that $K_{\alpha_1}$and K_{α_2}yields equal to 0.475 and 0.266, compared to 0.476 and 0.264 in our derivation, respectively.

The same derivation may be conducted for internal conversions of L-shell electrons. Following internal conversion of the L-shell, X rays and Auger electrons are radiated in the range 4–8.5 keV, with main lines:

- L_{α_1}- X ray with energy $E_{L_{\alpha_1}} = 6.1$ keV (transition from M_5 to L_3) ;
- L_{β_1}- X ray with energy $E_{L_{\beta_1}} = 6.7$ keV (transition from M_4 to L_2) ;
- $L_{\beta_{2,15}}$- X ray with energy $E_{L_{\beta_{2,15}}} = 7.1$ keV (transition from N_4 and N_5 to L_3) ;
- L_{γ_1}- X ray with energy $E_{L_{\gamma_1}} = 7.8$ keV (transition N_4 and L_2) ;
- Le^- - Auger electron with energy E_{Le^-} = 4.8 keV.

Auger yield for Le^- is one order of magnitude lower than for Ke^-, and the incertitude attached is approximately 25% [51]. Indicative emission rates per L-shell electron internal conversion are given in Table 5.

The average emission rates per Gd (n,γ) capture associated with the main X rays (*XR*), internal conversion (ICe^-), and Auger (Ae^-) electrons are summarized in Table 6, with the isotopic origin of the reaction product being mentioned. We emphasize the significant contribution from the X-ray term to the low-energy photon source term: Gräfe et al. [43] calculated a ratio of 1.32 between the sum of $K_{\alpha_1}$and K_{α_1}contributions and the 181.931 keV ray, comparable to the 1.23 ratio hereby derived, after ponderation by the 81.5% statistical weight of $^{157}_{64}$Gd (n,γ) reaction per Gd (n,γ) capture.

Radiation	K_{α_1}	K_{α_2}	K_{β_1}	K_{β_2}	Ke^-	$E_{L_{\alpha_1}}$	$E_{L_{\beta_1}}$	$E_{L_{\beta_{2,15}}}$	$E_{L_{\gamma_1}}$	Le^-
Emission yield	**0.476**	**0.264**	**0.147**	**0.042**	**0.077**	**0.171**	**0.106**	**0.036**	**0.019**	**0.668**

Table 5. X-ray and Auger electron emission yield per internal conversion.

Energy of reaction product (keV)	**Emission rate (nc^{-1})**	**Nature of reaction product**
4.8	**0.207**	Ae^- (**L-shell**)
6.1	0.053	$XR(L_{\alpha_1})$
6.7	0.033	$XR(L_{\beta_1})$
7.1	0.011	$XR(L_{\beta_{2,15}})$
7.8	0.006	$XR(L_{\gamma_1})$
29.3	0.166	ICe^- (Gd-157)

34.9	0.077	*Ae*$^-$ (K-shell)
38.73	0.044	*ICe*$^-$ (Gd-155)
42.3	0.264	*XR*(K_{α_2})
43.0	0.476	*XR*(K_{α_1})
48.7	0.147	*XR*(K_{β_1})
50.0	0.042	*XR*(K_{β_2})
71.9	0.248	*ICe*$^-$ (Gd-157)
77.9	0.059	*ICe*$^-$ (Gd-157)
81.3	0.051	*ICe*$^-$ (Gd-155)
131.7	0.030	*ICe*$^-$ (Gd-157)
149.0	0.006	*ICe*$^-$ (Gd-155)
174.1	0.011	*ICe*$^-$ (Gd-157)
180.1	0.003	*ICe*$^-$ (Gd-157)

Table 6. Prominent internal conversion electrons, X rays and Auger electrons after Gd (n,γ) capture.

3.3.4. Signal of interest for thermal neutron detection and counting

The overview of the radiative cascade following thermal neutron capture by Gd nuclei drives the exploitation of the σ cross section toward three main strategies:

- A detection scheme based on the signature of low-energy Auger and internal conversion electron in the 4–200 keV range. This signature is exploitable in gaseous detectors with powerful gamma-background rejection;
- A detection scheme based on the signature of medium-energy intense gamma-ray lines, X rays and internal conversion electrons in the 40–200 keV range. This signature will be identifiable in moderate-volume (up to a few cm^3) solid-state sensors, either scintillators or semiconductors. A higher gamma rate in such detectors will, however, require a compensation of the natural or radiological photon background over this energy range;
- A detection scheme based on the higher-energy gamma continuum between 200 keV and 8 MeV. The deposition of a significant part of these reaction products requires a high-density and/or high-volume sensor. It however allows for a favorable signal-to-noise ratio (SNR) above an energy threshold of 2.6 MeV, which exceeds the most-energetic gamma rays in the natural U-235, U-238 and Th-232 disintegration chains.

This subdivision of the Gd(n,γ) cascade into these privileged regions of interest corresponds to dedicated detection designs and optimizations, whose current status will form the topic of the rest of this paper.

4. Low-energy electron signature (4–200 keV) in gaseous detectors

Gadolinium is a powerful neutron absorber, converting the incident radiation into a set of cascade reaction products which directly (electrons) or indirectly (photons) ionize the detection medium, generating a nuclear counting signal. The Gd converter may be inserted into the sensing medium in two ways:

- Homogeneously dispersed or loaded inside the sensor, in the fields of semiconductor and scintillator-based detectors;
- As a cover on top of the sensor or interleaved with it, in the form of Gd layers, deposits or foils, in the fields of gaseous, semiconductor and large plastic detectors.

In the case of gaseous detectors, Gd converters must be deployed as solid-state layers, which have intrinsically lower geometrical efficiency than homogeneously dispersed solutions. The principle of the detection scheme, formulated by Jeavons et al. [52] includes, from outer to inner shells:

- A Gd-foil neutron converter into a low-energy, Auger and internal conversion electron source term, with energy lying between 4 and 200 keV according to Table 4;
- A high-density drift space, limiting the range of Gd (n,γ) cascade electrons;
- A multiwire proportional chamber (MWPC), which is a type of proportional counter with fine wires tensioned between two ground-potential, metal plates, and a noble gas where electron–ion pairs, generated along the track of the electrons, migrate under a several kV-electric potential difference.

The purpose of the high-density band is to allow for a position-sensitive neutron detection: a given cathode–anode pair provides *(x,y)* coordinates of the Gd-converter interaction with incident radiation. Key factors of merit for such gaseous, position-sensitive neutron detectors are:

- *Detection* or *registration efficiency*, defined as the ratio, expressed in %, of neutrons absorbed in the cover and giving rise to detectable electrons, either in the same direction as incident neutron radiation or opposite, to total incoming neutrons;
- *Two-dimensional spatial resolution*, defined as the minimum distance, expressed in mm, between neutron sources resulting in separate *(x,y)* coordinates at the output of the neutron detector;
- *Background*, defined as the false count rate, expressed in cps or cps. cm^{-2}, in the absence of a neutron emitter.

Interesting features also include the noble gas mixture used in the chamber, the type (natural or Gd-157 enriched) and thickness (in µm) of the converter, and the active or sensitive area (in cm^2). The main factors of merit reported in the previous study [52] are mentioned in Table 7.

From this basic detection concept, several upgrades have been proposed, notably through the introduction of a multistep avalanche chamber (MSAC) as an alternative to MWPC. In such a detector, the solid-state electron collimator mentioned *supra*, which generates a modulation of neutron signature directionality and increases gamma background, is replaced by an additional gas amplification stage. Merchart et al. [53] thus accessed superior performance in terms of spatial resolution, with similar figures of merit as far as efficiency and background vulnerability are concerned, also given in Table 6. Abdushukurov et al. [54] investigated mathematically the design of an one-dimensional (1D) position-sensitive neutron detector based on two MSACs with a natural Gd plane in between. The Gd converter thickness is optimized with regard to the registration efficiency of the internal conversion signature between 29.3 and 200 keV, with a mean around 70 keV. With a 10°angle between the detector and the 1.8 Å incident neutron beam, a 55-% efficiency is expected for a 3-µm natural Gd converter, *i.e.* more than twice the figure of merit of previously described configurations. The authors have then validated the modeled registration efficiency by comparison with experimental data from the Atominstitut (Vienna) and the Institut Laue Langevin (Grenoble) [55].

Two-dimensional (2D) position sensitivity forms a high goal in the development of gas chamber neutron sensors. Masaoka et al. [56] have thus described the Monte Carlo simulation-based optimization of a micro-strip gas chamber. In such a configuration, 2D localization is accessed thanks to a 1-mm thick lead glass plate with 100-µm wide cylindrical capillaries set at a distance d from the Gd converter. Primary internal conversion electrons and related secondary electrons then drift along the avalanche region and are collected in a printed network of 10 µm anode and 100 µm cathode strips. Spatial resolution is improved by a dense electron diffusion medium, in the form of a 1 µm-thick cesium iodide (CsI) layer, on the back of the Gd converter: one primary internal conversion electron with a mean energy of 70 keV is converted by recoil in a mean number of 10 electrons above 50 eV, multiplied in the avalanche region. In this context, secondary electrons from Compton diffusions of the gamma-ray, prominent signature of Gd (n,γ) captures, form a source of spatial resolution degradation and are therefore treated as a noise. The authors then describe an optimization

of the chamber design, with d = 100 µm and gas pressure of 0.02 atm, and associated figures of merit reported in Table 7.

Although they exhibit high registration efficiency and spatial resolution, the gaseous detectors reviewed in this section are essentially dedicated to fundamental investigations. Their absolute neutron sensitivity, notably lowered by the limited electron-stopping power of the gas and negligible attenuation of the prominent, gamma-ray signature of Gd (n,γ) captures, indeed forbids their deployment in field radioprotection and security applications.

	Detection efficiency (%)	**Spatial resolution**	**Background (cps. cm^{-2})**	**Gd composition**	**Gd thickness (µm)**	**Noble gas mixture (%)**	**Active area (mm^2)**
Jeavons et al. [52]	**22 % (1.8 Å, thermal)**	**1 mm (angles between 0 and 30°)**	**<1 (5 mm lead shield)**	**Natural**	**25**	**Isobutane (100 %)**	**4 × 4**
Melchart et al. [53]	~20 % (2.4 Å, thermal)	~0.7 mm FWHM (angles between 0 and 30°	<1 (5 cm lead shield)	Natural (Gd-157 modeled)	10	Ar (98 %), Acetone (2 %)	10×10
Abdushukurov et al. [54]	32–59 % (1.8 Å, thermal)	0.4 µm-1D (angle 10°)	-	Natural (90% Gd-157 tested)	3	Isobutane (100 %)	(200–350) ×10
Masaoka et al. [56]	26 %	160 µm-2D	n/γ ratio: 200	Natural	5	Ar (95 %), N_2 (5%)	-

Table 7. Figures of merit for Gd-based, gaseous neutron detectors.

5. Medium-energy gamma-ray, X-ray, and electron signature (40–200 keV) in small-volume, solid-state detectors

5.1. Gd-covered semiconductors

The development of light, portable detectors addressing active and personal neutron dosimetry forms a living topic of research in contemporary instrumentation for radioprotection. In this context, semiconductor technologies are favored, because of the high electron-stopping power and photon attenuation of dense solids, limiting the volume needed for an indirect neutron signature to be collected. Superior spectroscopic performance of the associated sensors also allows the identification of characteristic peaks. Like previously, the approach consists in covering an efficient photon and electron radiation sensor with a Gd layer, converting thermal neutrons into emissions that result in a series of well-defined energy peaks marked in Fig. 4 and Table 6.

The adjunction of a thin conversion layer to a pMOSFET diode, working as a current mode radiation detector, has been reported by Lee et al., first in the form of a metal Gd-cover [57], and then as a 0.5-µm thick sputtered deposit [58]. Such diodes implement a 2-µm gate oxide layer between the P-type layer and the Gd cover, in which the ionizing Gd (n,γ) reaction products lead to the creation of defects (trapped electrons and holes). The consequence is an increase in the diode threshold voltage as a function of neutron dose rate. The *linearity* of this relationship was experimentally validated up to 10 Gy. Key factors of merit for neutron counters and dosimeters include *neutron sensitivity*, *gamma background sensitivity* and either *neutron-to-gamma (n/γ) ratio* or *neutron detection limit* in a gamma-ray field. For this threshold shift-based detector, sensitivities are expressed in mV.cGy^{-1} and reported

in Table 8. The linearity of this shift with gamma background dose allows for a *compensation* of this false signal by subtraction of a baseline voltage shift, computed from a priori on the gamma background dose. An implementation of this detection scheme has been described by Vitale et al. [59], where the semiconductor is a fully depleted silicon-on-insulator (FDSOI) MOSFET with a thinner 2.5-nm gate oxide (SiO_2). Theoretical calculations, derived from the original model by McGregor et al. [60], have shown optimal thicknesses in the vicinity of 3 µm for a $^{nat}Gd_2O_3$ converter (registration efficiency: 17%) and 8 µm for a $^{157}Gd_2O_3$ converter (8%). Figures of merit are given for a 1-µm thick layer, considering a maximum, theoretical detection efficiency of 2.5%. In both cases, the ionizing signature is almost exclusively attributable to 70 to 200 keV internal conversion electrons, because of the limited size of detectors. A 10-% Gd-loaded HfO_2 coating, applied to an n-type Si heterojunction, has been described by Blasy [61]: the detector works in pulse mode, and neutron dose estimation is based on the area between two characteristic Gd (n,γ) peaks: 72 keV (Gd-158 internal conversion electrons) and 79.5 keV (Gd-158 gamma ray). The identification of both peaks is only accessible after subtraction of the background spectrum, acquired separately.

Aside from Si semiconductors, the intrinsic properties of sizeable, cadmium telluride (CdTe) crystals for neutron detection have been highlighted by Fasasi et al. [62]. On this basis, Miyake et al. [63] described an efficient scheme, in the form of pixelated Gd-covered CdTe diodes, with the purpose of taking advantage of both Gd and Cd neutron captures. The optimum for the Gd thickness was estimated by GEANT4 simulation in the vicinity of 25 µm. Measurements conducted with a 4×4×0.5 mm CdTe pixel in presence of a thermalized and shielded Cf-252 source have allowed for the identification of the characteristic X-ray peaks at 43 keV and 49 keV from Gd, prompt gamma-ray peaks at 79.5 and 182 keV from ^{157} Gd (n,γ) reactions, and gamma-ray peaks reactions at 88 and 199 keV from ^{155} Gd (n,γ) reactions.

Because of low-efficiency or the necessity of prior knowledge on the background spectrum to be subtracted, most of the mentioned schemes do not appear readily operable in real-time (response time between 2 s and 5 min [64]), in the presence of a mixed n/γ field. The essential part of the exploitable prompt photon and electron signature lies indeed under 200 keV for semiconductors, within the same range as secondary electrons due to interactions with background photons of comparable energy. Neutron counting by peak-area estimation may thus become unreliable because of natural or artificial gamma-ray interferences, whose intensity and spectral distribution are likely to vary at any time. This issue is addressed in reference work with the implementation of two-sensor compensation schemes. Aoyama et al. [65], for instance, introduced a two-Si semiconductor compensation scheme, in which two distinct covers are used: a 25-µm Gd foil for the first detector and a Sn cover, chosen for its atomic number (Z=50), which is reasonably close to that of gadolinium (Z=64), for the second detector. A 2-mm Lucite layer is used to isolate the electron responses of both sensors to incident radiations; the subtraction of both spectral responses aims at isolating the peak signature of 72–88 keV internal conversion electrons. Counts are integrated on both channels between 40 and 92 keV to highlight this contribution. The relatively high-efficiency of this scheme allows for real-time (3 s) compensation of gamma-background, which is why its sensitivity is expressed in count per second per thermal neutron flux unit: cps/(n. $cm^{-2}.s^{-1}$), cps/nv or equivalently $c.n^{-1}.cm^2$. On the basis of the same principle, Dumazert et al. [66] described the modeling and experimental study of a Gd/Tb-based compensation scheme, designed with the purpose of isolating the entire Gd (n,γ) photon and electron signature between 60 and 300 keV. With the purpose of maximizing the detection efficiency, the authors selected a CdZnTe semiconductor with high density (5.78 g. cm^{-3}) and atomic number. The quantification of the prominent gamma-ray and X-ray signature is secured by the closest compensation available of the interactions between the Gd converter and background photon radiations (photoelectric effects, Compton diffusions). Now Tb presents a negligible cross-section for thermal neutron capture (σ_{Tb} = 23.3 b to be compared with σ_{Gd} = 48.8 kb), the closest electron stopping power and photon attenuation to the ones of Gd, in relation with relative densities (ρ_{Tb} = 8.23 $g.cm^{-3}$ to be compared to ρ_{Gd} = 7.901 $g.cm^{-3}$) and atomic numbers (Z_{Tb} = 65 against Z_{Gd} = 64). The results of the first measurement campaign have confirmed the rejection of Cs-137 background, and detection of a neutron activity of a moderated Cf-252 source, with figures of merit reported in Table 8. The same scheme was transposed by the authors in the field of plastic scintillation [67], with the replacement of

CdZnTe sensors by 0.8 wt% Bi-loaded scintillators. Similar properties were described, although with an estimated thermal neutron sensitivity lowered by a half an order of magnitude.

Back to the signature of internal conversion electrons from Table 6, Kandlakunta et al. [68] introduced a two head-to-tail Si-sensor scheme. One Si-sensor is coated with a 25-µm metal, Gd layer, while the other is left uncovered. A 350-µm thick high-density polyethylene (HDPE) layer stops the internal conversions from the Gd-covered sensor. The subtraction of both detector responses to a neutron field therefore isolates the Gd (n,γ) prompt electron signature between 40 and 200 keV. The feasibility on an online Co-57 background compensation has been established on the basis of spectral shape.

	Neutron sensitivity	Gamma sensitivity	n/γ ratio–detection limit	Semiconductor	Gd cover	Linearity	Background compensation	Peak identification
Lee et al. [58]	25 mV.cGy^{-1} (thermal)	0.4 mV.cGy^{-1}	Rejection ratio: 60 (up to 210 Gy-300 Gy.h^{-1} ^{60}Co)	Boron-doped pMOSFET with gate oxide	0.5 µm (Natural Gd)	Up to 10 Gy	^{60}Co, with *a priori* on the dose	No
Vitale et al. [59]	6.6 V.n^{-1}. cm^2 (thermal)	-	Detection limit: 10^7 n. cm^{-2} (thermal)	FDSOI MOSFET	1 µm ($^{nat}Gd_2O_3$)	-	-	No
Blasy [61]	1.36.10^{11} c.n^{-1} (72 keV) 1.8 10^{11} c.n^{-1} (79.5 keV)	-	Detection limit: 2.10^{14} n.cm^{-2}	n-type Si heterojunction	500 µm(10 %-doped HfO_2)	-	Subtraction *a posteriori*	Yes (72, 79.5) keV
Miyake et al. [63]	-	-	-	p-type CdTe	25 µm (Natural Gd)	-	-	Yes (43, 49, 79.5, 88, 180, 199) keV
Aoyama et al. [65]	5.7.10^{-2} cps/nv	After compensation:-1.6 cps.µSv^{-1}.h (^{60}Co), -1 cps.µSv^{-1}.h (^{241}Am), 2.4 cps.µSv^{-1}.h (^{137}Cs)	Detection limit: 9 10^2 n. cm^{-2} (25 µSv.h^{-1} γ-background)	2 Si-PIN photodiodes	25 µm (Natural Gd)	Up to 500 nv	Real-time (within 3 s)	Significant contributions between 60 and 90 keV
Dumazert et al. [66]	3.6 10^{-1} cps/nv	After compensation:-9.8 10^{-2} cps.µSv^{-1}.h (^{137}Cs)	-	2 p-type CdZnTe	25 µm (Natural Gd)	-	Within 300 s	Significant contributions between 60 and 155 keV
Kandlakunta et al. [68]	-	-	Detection limit:8.6 10^4 n. cm^{-2}.s^{-1} (0.25 mSv.h^{-1} γ-bacground)	2 Si sensors	25 µm (Natural Gd)	-	Feasibility established (^{57}Co)	Yes (72, 131) keV

Table 8. Figures of merit for Gd-covered semiconductor detectors.

5.2. Gd-loaded scintillators

Compared to coating techniques, the interest of Gd loading lies within the maximization of the (n,γ) interaction rate, as well as the amplitude of the signature, for a given mass of the incorporated element. Inorganic Gd-scintillators, such as Ce^{3+}-doped GdI_3 crystals [69], have been described to have excellent light yield (expressed in photon per megaelectronvolt, ph/MeV) and neutron response under exposition to a moderated Cf-252 source, as reported in Table 9. Out of scalability, shape versatility and manufacturing cost considerations, however, the incorporation of Gd in plastic scintillators is more common, either by homogeneous or heterogeneous loading.

Plastic loading with heavy elements, such as Gd, is mainly limited by the lack of solubility of such dopants into the hydrocarbon-based solvent [70]. This drawback may lead to the degradation of the material's optical properties, notably through turbidity. For a homogeneous loading, the insertion of heavy elements in the form of organometallic compounds, with at least one covalent bond between the metal and the organic group (C, H, O), is required. Reference work by Czirr [71] presents the use of a Gd-benzoylacetonate (Gd $(HBa)_3$) complex for the loading of a commercial, polyvinyltoluene (PVT) NE120 scintillator (Nuclear Enterprises). Research was then undertaken to overcome the maximum 0.5 wt% load achieved by Czirr. Brudanin et al. [72] introduced the use of a hexamethylphosphotriamide (HMPT) co-dopant, which has enabled 3 wt% metal loading of polymethylmethacrylate (PMMA) under the form of Gd nitrate. A similar process has allowed Nemchenok et al. [73] to insert Gd up to 4 wt% with co-dopant hexamethylphosphoramide (HMPA) in PMMA. Expected registration efficiencies in both cases were estimated between 12% and 15% for neutrons below 500 meV. In recent work, preference was given to organometallic compounds with aromatic units, such as Gd-phenylcarboxylates investigated by Velmozhnaya et al. [74] in polystyrene (PS) matrices: gadolinium-5-phenylpentanate (Gd $(COO(CH_2)_4 C_6H_5)_3$ or Gd $(PhV)_{3)}$ with solubilizer triphenylphosphine oxide (TPPO) was inserted up to 50 wt% complex. With the aim of lowering manufacturing costs, Watanabe et al. [75] also reported a 0.1 wt% Gd-doped plastic scintillator in the form of a bisphenol A resin, hardened by the addition of an amine-based curing agent, and mixed with fluorophores and dopants at low temperature (below 60 C).

Reference work by Bell et al. [76] demonstrated the relevance of Gd-loaded PS for neutron detection. A PVT matrix was loaded up to 12 wt% with a tributylphosphate (TBP) complex of Gd nitrate (Gd $(NO_3)_3$), with satisfactory material (colorless samples) and optical (less than 50% light output degradation) features. Irradiation of 5 cm^3 samples by a 100 n. $cm^{-2}.s^{-1}$ thermal neutron flux (6.10^5 $n.s^{-1}$ Am–Li source behind a W shield) resulted in a response spectrum with discriminable peaks centered at 38 keV and 80 keV. The peaks are identifiable with a convolution of the main photon and electron signatures below 100 keV presented in Fig. 4 and Table 6. Additionally, the Gd complex described in the paper was found incorporable in silicone rubber.

A discriminable signal count rate attributable to a neutron emitter (moderated Cf-252 source) was also shown experimentally in the spectral response of

- A Gd-isopropoxide (Gd $[OCH(CH_3)_2]_3$)-loaded PS by Ovechnika et al. [77];
- A Gd-tétraméthylheptanedionate (Gd $(TMHD)_3$)-loaded PS by Bertrand et al. [78];

with associated characteristics reported in Table 8.

The Gd $(TMHD)_3$ complex was initially introduced in the loading of high-scale (10 m^3) liquid scintillators for neutron background suppression in power plants, and electron antineutrino detection experiments [79]. On the basis of the Gd-loaded samples described previously [78], the authors presented a two-scintillator scheme for online neutron detection [80] according to the principles exposed before [65], [66]. Count rate induced by background gamma rays, falling into the same [20–200 keV] energy range as Gd (n,γ) signature, is compensated by the response of a 0.8 wt% Bi-loaded scintillator with same dimensions (Table 9), so that neutron sensitivity to a Cf-252 source may be computed. The compensation scheme was found efficient in the presence of high-energy gamma backgrounds (Cs-137, detection limit 0.15 n. $cm^{-2}.s^{-1}$) but unreliable for medium-energy backgrounds (Am-241), because of the discrepancy of Gd- and Bi-loaded scintillators' photoelectric responses within this range.

To achieve high mass loading or diversified neutron signature in plastic scintillators, heterogeneous doping of the matrix with Gd crystals represents another powerful approach. Cai et al. [81] thus claimed as high a Gd-mass load as 27 wt% in the form of 9×9×1 nm Gd_2O_3 nanocrystals embedded in a PVT matrix, with excellent light yield and spectroscopic features up to 662 keV (γ). These modified polymers have, however, not been studied yet for thermal neutron detection.

A composite neutron dosimeter, formed by 300 to 500 µm, Ce^{3+}-doped lithium gadolinium borate ($Li_6Gd(BO_3)_3 : Ce^{3+}$) inorganic scintillators, dispersed in a plastic scintillator matrix, was introduced by Williams et al. [82]. Gadolinium is natural, while lithium and boron are enriched up to 95% in Li-6 and B-10 isotopes, respectively. Addressing neutron dosimetry requires the discrimination of pulses induced by neutrons interacting with the sensor according to the energy range of the particle. In this case, and according to our introduction:

- Pulses with long rise time, followed by a large-area pulse within 10 µs, are attributed to fast ($E_n \leq 1$ MeV) neutron-related $^1H(n,n')$ recoils in the PVT matrix, followed by $^6Li(n,\alpha)$ slowed neutron capture with 4.78 MeV Q-value;
- Pulses with a short rise time and an area corresponding to more than 2 MeV deposited energy are attributed to thermal (hereby defined by $E_n \leq 500$ meV *i.e.* below cadmium cut-off) neutron capture by Gd nuclei (with 8 MeV Q-value).

Tests under monoenergetic {144 ; 250 ; 565 ; 1200 ; 2500 ; 5000} keV and slow neutron irradiation by Williams showed performant fast/thermal neutron separation and gamma rejection up to 1 MeV neutron-energy sources, with thermal neutron sensitivity reported in Table 9. Recent work by Slaughter et al. [83] described a similar $^6Li_6\ ^{nat}Gd\ (^{10}BO_3)_3 : Ce^{3+}$-based sensor. The active capacity was scaled up to 1.3 l, and the LGB:Ce microcrystal load inside the PVT matrix reached 10 wt%. Like previously, pulses are classified in a three-category typology (neutron diffusion event, neutron capture event and gamma-ray event), on the basis of pulse shape and time-to-capture (12 µs, in this case, between proton recoil and subsequent capture). The authors highlighted the ability of the detector to resolve neutron energies between 0.8 MeV to 150 MeV with regards to the respective contributions of so-discriminated events.

	Matrix	Dopant	wt% Gd	Dimensions	Light yield	Neutron response
Glodo et al. [69]	GdI_3 :Ce^{3+}	-	29 (Matrix)	10×20×1 mm	58000 ph/MeV	Peak at 86 ±25 keV :5000 Ph/detected neutron
Czirr [71]	PVT	Gd $(HBa)_3$ (homogeneous)	0.1–0.5	2.54 (ø) × 15.24 cm	15%–42% of unloaded NE120 (0.1–0.2 wt% Gd)	-
Brudanin et al. [72]	PMMA	Gd $(NO_3)_3$ (homogeneous)	3	30 (ø) ×10 mm	51% of unloaded plastic scintillator	-
Nemchenok et al. [73]	PMMA	GdCl3 (homogeneous)	4	27 (ø) × 10 mm	67.6% of unloaded plastic scintillator	-
Velmozhnaya et al. [74]	PS	Gd $(PhV)_3$ (homogeneous)	4	-	60% of unloaded plastic scintillator	-
Watanabe et al. [75]	Bisphenol A resin	Unknown dopant	0.1	20 × 200 × 3 mm	56.5% of unloaded plastic scintillator ~700 ph/MeV	
Bell et al. [76]	PVT	Gd $(NO_3)_3$ $(TBP)_3$	1.5	2.5 (ø) × 1 cm	60% of unloaded plastic scintillator (1 wt% Gd)	Peaks at 38 ± 10 keV and 80 ± 15 keV
Ovechnika et al. [77]	PS	Gd $[OCH(CH_3)_2]_3$ (homogeneous)	2.5	14 (ø) × 6 mm	76% of unloaded plastic scintillator	Peak at 70 ± 20 keV
Bertrand et al. [78]	PS	Gd $(TMHD)_3$ (homogeneous)	2	16 (ø) × 8 mm	50% of unloaded plastic scintillator ~ 5000 ph/MeV	Signature distributed between 20 and 200 keV Sensitivity (0.8 wt% Bi-loaded compensator): $3.3.10^{-1}$ cps/nv
Cai et al. [81]	PVT	Gd_2O_3 (heterogeneous)	27	14 (ø) × 3 mm	27000 ph/MeV	-
Williams et al. [82]	PVT	Li_6 Gd $(BO_3)_3$: Ce^{3+} (heterogeneous)	-	5.08 (ø) × 3.81 cm	-	9.64 10^{-2} $c.n^{-1}.cm^{-2}$ from Gd (thermal)
Slaughter et al. [83]	PVT	Li_6 Gd $(BO_3)_3$: Ce^{3+} (heterogeneous)	10 (LGB:Ce)	12.7 (ø) × 10.2 cm	-	Neutron dosimetry between 0.8 and 150 MeV with ±8% rate uncertainty

Table 9. Figures of merit for Gd-loaded scintillators.

6. High-energy gamma-ray signature (2–8 MeV) in large-scale liquid and solid detectors

The detection schemes presented in Sections 4 Low-energy electron signature (4–200 keV) in gaseous detectors, 5 Medium-energy gamma-ray, X-ray, and electron signature (40–200 keV) in small-volume, solid-state detectors make use of the low- and medium-energy signature of thermal neutron captures in moderate-volume sensors (up to 75 cm^3). The last reference by Williams et al. shows that, as the gamma-sensitive volume increases, the high-energy gamma-ray tail of the de-excitation spectra illustrated in Fig. 3, Fig. 4 becomes exploitable. A promising strategy then is to quantify the prompt de-excitation signal above the 2.614 MeV upper relevance threshold [84] of natural background radioactivity (Tl-208). To significantly attenuate photons above 3 MeV, the radiation sensor must be scaled up enough, with regards to a tradeoff between cost and detection efficiency. This last consideration tends to drive the solutions toward liquid- and plastic-based technologies. Orders of magnitude for the length scale required to capture a useful fraction of this high-energy gamma-ray signature are calculated with gamma attenuation coefficients from the National Institute of Standards and Technology database [85]. For liquid and plastic scintillators, typical range-absorption yield relations for a 3 MeV photon are: 33% in 10 cm, 50% in 17.5 cm, 67% in 28 cm, and 90% in 58 cm.

6.1. Liquid detectors

In the field of material characterization by (γ,n) photofission, Beil et al. [86] designed a very-large-scale neutron counter based on a 0.5 wt% Gd-loaded commercial, xylene (C_8H_{10}) NE323 (Nuclear Enterprises) liquid scintillator. Monte Carlo calculations have shown 60% to 85% registration efficiency, in accordance to a tradeoff between neutron capture and gamma background.

Xylene-based scintillators induce safety hazards because of potential toxic matter leakage and relatively low-temperature flash point (38 C for NE323). As a consequence, considerable effort went over the last decade into less flammable and less toxic chemical formulations, to work large-scale liquid scintillators into practical homogeneous detection media. This research was notably carried out in the framework of reactor antineutrino experiments. In this context, antineutrinos first interact with hydrogen, present in large amount inside the target, according to the inverse beta decay reaction equation:

$$ {}^{0}_{0}\overline{\nu_e} + {}^{1}_{1}p^{+} \rightarrow {}^{1}_{0}n + {}^{0}_{1}\beta^{+} \qquad (11) $$

An antineutrino ${}^{0}_{0}\overline{\nu_e}$ is thus detected through the annihilation of the β^+ positron and the delayed capture of the neutron ${}^{1}_{0}n$, with the temporal correlation of both signals increasing the ratio between antineutrino signature and random background. Loading Gd in the liquid scintillator devoted to neutron counting has been found to significantly reduce the mean time gap between antineutrino reaction and neutron capture, therefore increasing the correlation frequency rate and lowering the false detection background. We have mentioned, in paragraph 5.2, the use of a Gd $(TMHD)_3$ organometallic compound to load high-scale liquid scintillators as introduced by Aberle et al. [79]. The preparation, developed in the frame of the Double Chooz reactor antineutrino experiment, was based on a linear dodecane ($C_{12}H_{26}$, 80%) solvent mixed with ortho-phenylxylylethane (o-PXE, $C_{16}H_{18}$, 20%), and showed high attenuation length at 430 nm (7.8 ± 0.5 m), a critical feature for the collection of the scintillation signal in a large-scale radiation sensor. Background is kept below 1% of the expected neutron signal by applying a frequency high-pass filter, with a threshold at 10 Hz, on the count rate. In the course of the Daya Bay reactor antineutrino experiment, Beriguete et al. [87] also reported the production and characterization of a 185-tonne, 0.1-wt% doped liquid scintillator based on a linear alkylbenzene (LAB, $C_6H_5C_nH_{2n+1,10\leq n\leq 16}$) solvent and a trimethylhexanoic acid (TMHA) ligand to load Gd. Both preparations proved higher stability (investigated with help of Am–Be and Pu–C neutron sources for the second scintillator), lower toxicity, higher flash points (74 C for dodecane, 140 C for LAB), and producibility in larger quantities than xylene-based references. Recently, as part of the Neutrino Oscillation at Short baseline experiment, Kim et al. [88] introduced a 0.5-wt% Gd-loaded liquid scintillator with a composite solvent: 90% is LAB and 10% is di-isopropylnaphtalene (DIN, $C_{16}H_{20}$), that was shown to increase the light output compared to the original preparation in reference [87]. Another valuable feature from LAB/DIN scintillator with Gd $(TMHA)_3$ is good

discrimination between neutron recoil and gamma discrimination above 500 photoelectrons collected from the interaction. We recall that this discrimination is based on different shapes of pulses in the time domain: proton recoil pulses from fast neutrons have a higher ratio of charge below the tail of the pulse over total charge of the pulse than electron recoil pulses from gamma rays.

As an alternative to Gd-loaded scintillators, Dazeley et al. [89] investigated another high-scale liquid detector, in the form of a 250-L, 0.2-wt% $GdCl_3$-doped water Cherenkov tank. A set of 8 UV-sensitive photomultiplier tubes allows for a resulting 10-% collection efficiency of Cherenkov photons. The signature above 3 MeV equivalent is filtered in the event-frequency space on the basis of an expected inter-neutron capture period of about 28 µs. This spectral treatment allows for a rejection of high-energy fission gamma rays (such as the prompt gamma rays from Cf-252 spontaneous fissions, used in the experimental study) and background. Only spallation neutrons from the natural muon shower and undergoing capture form a background that cannot be discriminated in the frequency space from the Cf-252 source Gd (n,γ) signature. The concept of this very-large-scale neutron was transposed to the field of SNM passive detection by means of a GEANT4-based optimization study [90]. The aim of the study is to design 1-tonne water Cherenkov modules covering a large solid angle. The counting algorithm aims at detecting time-correlated neutrons, *i.e.* multiple neutrons from a single fission (or even subsequent neutrons from fission chains in a weakly multiplying source), to reduce the rate of false alarms. The complete design of a module includes nine PMTs, a segmentation between a Gd-loaded region (1/5) and an unloaded region (4/5), and a top muon veto. A high-energy threshold (140 photoelectrons, corresponding to 2.6 MeV gamma ray total absorption) accounts for gamma background without pile-up, and the detector segmentation serves the rejection of spallation neutron detection. With a frequency threshold at 130 Hz over triggering events, a 4-module water Cherenkov system with a 0.6 wt% $GdCl_3$ load is expected to have a 25% registration efficiency and a detection limit of 75 g of plutonium within 20 s. The prescriptions of the authors were implemented in a full-size module prototype by Dazeley et al. [91]: 8 PMTs with a 10-inch diameter were positioned on top of a 121.9 × 91.4 × 119.4 cm^3 stainless steel tank containing 1 tonne of Gd-doped water. The increase by a factor of 3 in $GdCl_3$ mass concentration from reference [89] lowers the mean neutron capture time from 28 µs down to 16 µs, and the inter-correlated neutron event period to 12.3 µs. For neutron coincidence counters, a specific figure of merit (noted FOM in Table 10) is defined [92] as the ratio between registration efficiency (here, 28% under low and medium-energy gamma-ray backgrounds) and the square root of the mean capture time, equal to 7%.$MHz^{1/2}$ in the case of the reviewed paper. Neutron registration efficiency of 22% in presence of Cf-252 under a 4 MBq gamma-ray background and neutron/Co-60 rejection factor of 10^8 below a 220 kBq gamma-ray background make the technology promising for SNM detection under real-life conditions.

	Radiation sensor	Gd converter	Dimensions	Neutron response	Detection limit/gamma rejection
Beil et al. [86]	Xylene-based liquid scintillator	0.5 wt% Gd-loaded	500 dm^3 ball	60% registration efficiency	n/γ ratio: ~ 16
Aberle et al. [79]	Dodecane/o-PXE-based liquid scintillator	0.123 ± 0.002 wt% Gd-loaded	20 m^3 over 2 scintillators	>80% registration efficiency	n/γ ratio :> 100 Spectral filtering above 10 Hz
Beriguete et al. [87]	LAB-based liquid scintillator	0.1 wt% Gd-loaded	185 tonnes over 8 antineutrino detectors (AD)	Stable over different ADs and over time	Spectral filtering (28.5 ± 0.2 µs inter-correlated event period) False count rate from radioactive impurities
Kim et al. [88]	90-% LAB/10-% DIN liquid scintillator	0.54 ± 0.03 wt% Gd-loaded	1000 L	High registration efficiency	Fast n/γ Pulse Shape Discrimination in the time domain
Dazeley et al. [89]	Ultra-pure, sterilized water	0.1 wt% Gd-loaded	100 × 50 × 50 cm^3	$2.5.10^5$ $n.s^{-1}$ Cf-252 source detected at 1 m (5 cm lead shied)	Spectral filtering (28 µs inter-correlated event period) False count rate from spallation neutrons and muons
Dazeley et al. [90], [91]	Pure 18 MΩ deionized water	0.5 wt% $GdCl_3$-loaded	1.02 m^3 tank	28 ± 0.5% registration efficiency and FOM = 7.0%.$MHz^{1/2}$ (Cf-252, Co-60 background under 220 kBq) 22 ± 1 % registration efficiency and FOM = 5.5 %.$MHz^{1/2}$ (Cf-252, Co-60-equivalent background up to 4 MBq) Minimum detectable neutron activity: 3.1 $n.s^{-1}$ (Cf-252)	n/γ ratio: 10^8 (Cs-137, Co-60 with activity below 220 kBq) Spectral filtering (12.3 µs inter-correlated event period) Stable background from cosmic rays

Table 10. Figures of merit for Gd-based large-scale liquid detectors.

6.2. Solid detectors

For detectors destined to be deployed in field applications, whether for radioprotection or security inspection, solid-state, mechanically robust, sealed and non-fusible media tend to be favored. As an illustration, RPMs set up to detect static or moving radio-emitters at critical checkpoints or in public places, must meet a double constraint: first, being as sensitive as possible to all potential radiations (gamma rays, neutrons), which requires a scale-up of smaller solid-state media, and, second, ensuring an acceptable tradeoff between registration efficiency and the cost of materials. These considerations have increasingly driven industrial solutions toward plastic scintillator-based monitors [93]. Because of the scale-up (up to 10 dm^3) undergone by the plastic scintillator, and following the discussion in paragraph 5.2, no loading is accessible and Gd needs to be introduced as a bulk or covering foil neutron converter. A principle patented by Richard [94] and consisting in wrapping inorganic scintillators within gadolinium foils to enhance neutron sensitivity was thus adapted to the design of a high-scale system where plastic scintillators form the radiation sensors. De Vita et al. [95] introduced a detection scheme taking advantage of Gd (n,γ) reactions in the 25 µm, Gd_2O_3 internal coating of 50-µm Mylar and 150-µm Tedlar foils, in which 200 × 6 × 6 cm^3 plastic scintillator bars are wrapped. These plastics bars play both roles of neutron moderators and detection medium sensitive to the prompt gamma-ray signature of thermal neutron captures up to 8 MeV. Both extremities of each plastic scintillator are coupled with a PMT to collect and convert the light output. Such coated blocks are concatenated in a 16 × 4 bar matrix, forming an overall 450 dm^3 radiation monitor. Neutron/gamma discrimination in this scheme is based on *hit multiplicity*, *i.e.* the number of isolated bars registering a signal after a neutron capture or a gamma diffusion event. The GEANT4 model of the system shows that, by setting a n/γ threshold on hit multiplicity equal to 3, a 28% theoretical neutron registration efficiency and 145 gamma-rejection ratio may be obtained. This concept was subsequently implemented in a versatile n/γ two-portal prototype developed in the frame of the FP7 SCINTILLA European project, according to a variant in which the scintillating blocks are interlined with similar Gd_2O_3-coated Mylar. Fanchini [96] has reported a 100-% detection rate for a Cf-252 source moderated by 4 cm of HDPE, with activity of 2.10^5 $n.s^{-1}$, and 90-% rate for 8 cm of HDPE and with activity of 1.3 10^5 $n.s^{-1}$, in both cases at a distance of 2.5 m from the monitors. The false neutron alarm rate, evaluated in the absence of Cf-252, was certified as null over 1000 transits up to a Cs-137 20 $\mu Sv.h^{-1}$ gamma dose rate. These test results are in compliance with the requirements of the ANSI N42.42 norm [97].

Large inhomogeneous-doped plastic scintillators have also received attention in the frame of fundamental research and laboratory experiments. Pawełczak et al. [98] reported a prototype of Neutron Sandwich Transmuter/Activation-γ Radiator (NSTAR) applied to the determination of neutron multiplicity in a deuterium–deuterium (DD), fusion-based neutron generator. The NSTAR module detects neutrons on the basis of a temporal correlation between first proton recoils along the neutron diffusion process and the delayed capture of thermalized neutrons by Gd-155 and Gd-157 nuclei. The prototype takes the form of a PMT-coupled, high-scale stack of parallelepipedic 10 × 20 × 2 cm^3, fast-decay plastic scintillators (Saint-Gobain, BC-408), interleaved with 1 mm-thick, Gd_2O_3-doped poly(-dimethyl-siloxane) (PDMS), *i.e.* a total 0.5 wt% inhomogeneous Gd load. With a temporal correlation window between 7 and 97 µs (for a mean neutron capture time, as defined in paragraph 6.1, of about 22 µs), and up to a 5 MeVee (MeV-electron equivalent) spectral signature, a neutron/gamma SNR of two to three orders of magnitude was obtained, advantageously comparing to SNR below half-an-order of magnitude by mere pulse height discrimination above 2.5 MeVee (*i.e.* the Tl-208 ray). The so-called *multi-hit capability*, *i.e.* the power of resolving multiple neutrons emitted in a burst, was tested with a 10 Hz-pulsed, MP320 small DD neutron generator: mean multiplicities of 3.4 ± 0.5, 9.5 ± 1.2 and 13.7 ± 1.7, were estimated for 30, 60 and 80µA-beam currents respectively, thus verifying a proportionality relation of about 0.15 ± 0.03 μA^{-1} (under up to a 7.10^{-4} $n.s^{-1}$ emission rate). Another noteworthy application once again relates to the counting of electron antineutrinos, this time as tool for the monitoring and control of nuclear power plant reactors. Indeed, unstable products from U-235 and Pu-239 fissions mostly decay through beta minus (β^-) disintegration, with an average of 6 antineutrinos per fission product beta-decay chain [99]. As an illustration, these add up to a $2.10^{20}\nu.s^{-1}$ electron antineutrino emission rate of about for an operating 1-GWt power plant. Aiming at this application, Kuroda et al. [100] introduced a mobile and adaptable Plastic AntiNeutrino Detector

Array (PANDA), whose material and algorithmic design is similar to the one described in reference [95]. The detector is based on 10 × 10 × 100 cm^3 plastic scintillator bars wrapped with Gd-coated (4.9 mg. cm^{-2}) Mylar films. The fine granularity of a several hundred-kg target built from the concatenation of such modules allows topological particle identification based on a hit-multiplicity gate. The detection algorithm discriminates antineutrino events on the basis of integral (over all modules) prompt energy above 3 MeV (*i.e*. above natural gamma-ray background energy), integral delayed energy between 3 and 8 MeV (hence targeting the background-discriminable gamma-ray signature of ^{155} Gd (n,γ) and ^{157} Gd (n,γ) capture reaction up their associated Q-values), and prompt-delayed time interval between and 6 and 200 µs (related to the mean capture, as previously detailed). Additional gates depend on the first and second maximum energy laid down in individual modules. Simulations announced a 4 to 11.6% antineutrino registration efficiency and an expected antineutrino rate between 15 and 270 event per day at 30 m from a 3 GWth reactor, for PANDA detectors ranging from 16 (160 kg) up to 100 (1 tonne) modules. A 360-kg prototype, said PANDA36, was then built and set at sea level within 36 m of the 3.4 GWth reactor of Ohi Power Station (Kansai Electric Power Co., Inc.), as reported by Oguri et al. [101]. A complex discrimination scheme, based on the topology of energy deposition, had to be implemented in these conditions of deployment. A *muon veto* is formed by the exclusion of events leading to more than 8 MeV deposited within 250 µs before the *delayed event*, which is identified with the capture of the neutron from Eq. (11) being captured in Gd. The prompt event, in the context of indirect antineutron detection, is caused by positron–electron annihilation of the first reaction product in Eq. (11). In the meantime, the capture by Gd nuclei of cosmogenic neutrons, generated by muon spallation, here forms a primary source time-correlated background, whenever fast neutron recoil followed by thermal neutron capture (correlated signature of a cosmogenic neutron) gets counted as positron annihilation followed by thermal neutron capture (correlated signature of an electron antineutrino). A discrimination is achieved by requiring an individual energy deposited in the second most sensitive bar below 520 keV (close to the 511-keV energy of a single annihilation ray) and a relation between the energy deposited in the first most sensitive bar (E_1), the energy deposited in the third most sensitive bar (E_3), and the total energy deposited in PANDA36 (E_{tot}) as:

$$\frac{E_3}{E_{tot}} \geq \frac{\frac{E_1}{E_{tot}} - 0.5}{5} \qquad (12)$$

Time window may be adjusted with respect to SNR maximization, with an upper boundary lying between 50 and 150 µs. A 22 ± 11 $c.day^{-1}$ count rate difference was obtained experimentally when the reactor went from ON to OFF state, consistent with the theoretical 3.4% antineutrino detection efficiency calculated by the authors.

We have previously seen that fixed, large-scale portal monitors based on plastic scintillators interleaved with Gd exhibit high neutron efficiency in realistic conditions of deployment. Dumazert et al. [102] studied the transposition of such a detection scheme to transportable systems, with dimensions ranging from 700 to 1300 cm^3. This scale corresponds to the standard of bulky, He-3 counters inserted at the center of HDPE's so-called Bonner spheres [103], which can be used by radioprotection practitioners in the field. The authors introduced a detection scheme including a bulk, metal Gd core enveloped by a 11.8-cm-radius plastic scintillator sphere. Incident fast neutrons are thermalized by the plastic and then captured by Gd-155 and Gd-157 nuclei in the core. The attenuation of a fraction of the Gd (n,γ) Q-value carried by high-energy gamma rays in the surrounding scintillator then leads to a significant count rate above 5 to 6 MeVee thresholds, which minimize other contributions to the signal (muons, high-energy fission gamma rays). A first prototype was prepared with a cross-linked PS matrix and irradiated with a Cf-252 source, set at a distance of 60 cm and behind a 10-cm lead shield. The first estimations of sensitivity and detection limits are reported in Table 9 and found within the same order of magnitude and half-an-order of magnitude above the performance of a commercial He-3 Bonner sphere, respectively; hence, it is compatible with the constraints of real-time efficient radioactivity monitoring. Recent developments [104] have described an evolution of this concept toward a hollow Gd core and two plastic scintillators with different time constants, allowing for online n/g and neutron/muon (n/µ) discrimination depending on temporally coincident Gd (n,γ) events in both sensors. To address neutron spectrometry and counting in the range

of 20 MeV to 1 GeV, on the other side, Roecker et al. [105] designed a 1-tonne pickup truck-transportable Multiplicity and Recoil Spectrometer (MARS). The counting of neutrons from 20 to 100 MeV is based on a capture-gated algorithm similar to the ones described in references [95], [98]: MARS includes two 100 × 75 × 25 cm^3 dual plastic scintillator/Gd blocks, each consisting of twelve 12-cm thick BC-408 bars interleaved with Gd-Mylar sheets. To address the detection of higher energy neutrons, a 101 × 71 × 20 cm^3 lead table is set between both blocks and acts a *spallation target*: very fast neutrons spall 1 to 2 MeV, lower-energy neutrons with a multiplicity depending on the incident energy. These secondary neutrons are then moderated in plastic and undergo Gd (n,γ) capture within a 19 ± 3 μs time delay. A multiplicity-based algorithm with an expendable delay window, validated with a neutron source of known emission multiplicity (Cf-252, 3.77 ± 0.02 neutrons per average spontaneous fission [106]), was found to reach a detection efficiency of 12.8 ± 0.1%. The MARS detector was expected to have an effective area ranging from 1800 to 2500 cm^2 for 20–100 MeV neutrons, and ranging from 500 to 5000 cm^2 for 100 MeV-1 GeV neutrons on the basis of GEANT4 simulations.

The key properties (radiation sensor, Gd homogeneousor heterogeneous loading, dimensions) and figures of merit (neutron sensitivity, background-rejection scheme and ratio, detection limit) for the detectors reviewed in this section are presented in Table 10 (liquid-state detection media) and Table 11 (solid-state detection media).

	Radiation sensor	Gd converter	Dimensions	Neutron response	Detection limit/gamma rejection
De Vita et al. [95] / Fanchini [96]	Standard plastic scintillators	25 µm Gd_2O_3 coating	200 × 96 × 24 cm^3 RPM	100 % detection of a 2.10^5 $n.s^{-1}$ Cf-252 source at 2.5 m (1 cm steel and 0.5 cm lead shields)	No false neutron alarm up to 20 $\mu Sv.h^{-1}$ γ (Cs-137)
Pawełczak et al. [98]	Fast-decay plastic scintillators (BC-408)	1 mm Gd_2O_3-doped PDMS films (total: 0.5 wt%)	10 × 20 × 50 cm^3 planar slab stack	26 ± 3% registration efficiency FOM = 5.6 ± 0.7%.$MHz^{1/2}$ Hit-multiplicity capability: 0.15 ± 0.03 μA^{-1}(DD neutrons)	n/γ ratio : between 10^2 and 10^3 for capture-gated (7–97 µs) counting
Kuroda et al. [100] / Oguri et al. [101]	Standard plastic scintillators (Rexon RP-408)	25 µm Gd_2O_3 coating of polyester	36 modules of 10 × 10 × 100 cm^3 360 ± 18 kg (PANDA36)	Electron antineutrino detection efficiency: 3.15 ± 0.93% Count rate difference over the shutdown of a 3.4 ± 0.1 GWth reactor at a distance of 35.9 ± 0.1 m: 21.8 ± 11.4 $c.day^{-1}$ (7 days)	300 to 400 $c.day^{-1}$background from cosmogenic muon and spallation fast neutrons
Dumazert et al. [102]	Cross-linked PS	8.4 g bulk Gd	6.88 dm^3 ball	Sensitivity: 0.08–0.14 $c.n^{-1}.cm^{-2}$ (Cf-252 with 10 cm lead shield, counting thresholds 5–6 MeVee)	Detection limit: 8–10 $n.cm^{-2}.s^{-1}$ over 60 s (up to 30 $\mu Sv.h^{-1}$ Cs-137 and Co-60)
Roecker et al. [105]	Fast-decay plastic scintillators (BC-408)	Gd-coated Mylar sheets	Two 100 × 75 × 25 cm^3 PS/Gd blocks Central 101 × 71 × 20 cm^3 lead table	Effective area between 1800 and 2500 cm^2 for 20–100 MeV neutrons Effective area between 500 and 5000 cm^2 for 100 MeV–1 GeV	Fixed time delay (65 µs) capture-gated discrimination (20–100 MeV neutrons) Adjustable time delay capture and multiplicity-gated discrimination (100 MeV–1 GeV)

Table 11. Figures of merit for Gd-based large-scale solid detectors.

7. Conclusion

Gadolinium is a stable, naturally occurring element with the highest interaction probability with neutrons at thermal energy; the neutron capture is followed by a radiative rearrangement of nuclear and atomic structures. Depending on the nature and energy of the reaction products that a Gd-coated or loaded detector aims at isolating as the radiative signature of neutron captures, dedicated sensors and counting methods have been introduced over the last decades. Gd-covered gaseous detectors, with inherent low photon background vulnerability, have been designed to provide a localized detection, down to 100µm in two dimensions, of low-energy (4–200 keV) Auger and internal conversion electrons. Medium-energy (30–100 keV) internal conversion electrons have been highlighted as a neutron capture signature in Gd-covered semiconductors, notably Si, CdTe and CdZnTe, with sensitivities reaching 10^{-2} – 10^{-1} cps/nv. However, these solid-state media sensors present higher gamma background than gas, Compton diffusion, and photoelectric electrons contributing to the signal over the same energy range. This issue is addressed in two-sensor compensation schemes, using a Sn, Tb or HDPE compensator of the 25 µm-Gd neutron converter, and detection limits in a mixed field lowered to 10^{3} – 10^{1} n.cm^{-2}. With similar compensation schemes for online background compensation, Gd-loaded and covered plastic scintillators have been described, which are more easily scalable and therefore suited for collecting the medium-energy (40–200 keV) X-ray and gamma-ray signature of Gd (n,γ) captures. Eventually, large-scale Gd-loaded liquid detectors, and plastic scintillators interlined or weighted with metal Gd have been deployed as sensitive media to the high-energy (3 MeV-8 MeV) component of the prompt emission following neutron capture. Ranging from 1 to 100 dm^3 volumes, this type of plastic sensor has shown sensitivities equivalent to He-3 Bonner sphere standards and compliance with internationals norms related to RPM. Online gamma rejection forms a crucial technical issue, allowed by a temporal or spectral filtering of Gd-implemented radiation sensors exploiting discriminable signatures. The inventory drawn in this paper highlights that recent developments have proven to be compatible with the requirements of real-time, limited-dose (up to 100 mSv.h^{-1}) background deployment, in terms of neutron sensitivity, neutron detection limit in a mixed n/γ field, and transportability, whether moderation is intrinsic or extrinsic. The next challenge that such solutions will have to address is to ensure real-time, unambiguous neutron detection is a gamma background exceeding 100 µSv.h^{-1} dose rate, and provide dosimetric information on the detected neutron spectrum according to the H*(10) norm definition [107]. For this purpose, promising paths for Gd-based neutron detection have been opened in contemporary instrumentation, and pursued through academic research, industrial collaborations and international projects.

References

[1] Burel J.-P. Instrumentation hors cœur des réacteurs. Techniques de l'Ingénieur, 3 (1999), p. 451

[2] Endo K. Radiation protection at nuclear fuel cycle facilities. Radiat. Prot. Dosim., 146 (1–3) (2011), pp. 119-122

[3] Knoll G. Radiation Detection and Measurement (fourth ed.), John Wiley & Sons, Inc., New York (2010), pp. 19-26

[4] Lyoussi A. Mesure nucléaire non destructive dans le cycle du combustible. Partie 1. Techniques de l'Ingénieur, 3 (2005), p. 405

[5] Runkle R.C., Bernstein A., Vanier P.E. Securing special nuclear material: Recent advances in neutron detection and their role in non-proliferation. J. Appl. Phys., 108 (11) (2010), pp. 1101-1121

[6] Crane T.W., Baker M, P. Neutron Detectors, Passive Non-destructive Assay of Nuclear Material, National Technical Information Service, Springfield VA (1991), pp. 79-406

[7] Beckurts K.-H., Wirtz K. Neutrons Physics, Springer-Verlag Berlin Heidelberg GmbH (1964), pp. 59-61

[8] Klett A., Burgkhardt B. The new remcounter LB 6411: Measurement of neutron ambient dose equivalent H*(10) according to ICRP60 [with high sensitivity]. IEEE Trans. Nucl. Sci., 44 (3) (1997), pp. 757-759

[9] Shea D.A. The helium-3 shortage: Supply demand and options for Congress, Congressional Research Service (2010)

[10] Managing critical isotopes, weaknesses in DOE's management of helium-3 delayed the federal response to a critical supply shortage, GAO-11-472, U.S. Government Accountability Office, Washington, D.C. (2011).

[11] Berglund M., Wieser M.E.c Isotopic compositions of the elements 2009 (IUPAC Technical Report). Pure Appl. Chem., 83 (2) (2011), pp. 397-410

[12] MacDonald M.R., Bates J.E., Ziller J.W., Furche F., Evans W.J. Completing the series of +2 ions for the lanthanide elements: Synthesis of molecular complexes of Pr^{2+}, Gd^{2+}, Tb^{2+}, and Lu^{2+}. J. Am. Chem. Soc., 135 (26) (2013), pp. 9857-9869

[13] Stwertka A. A Guide to the Elements (second ed.), Oxford University Press, Inc. (2002), p. 157

[14] Ganjali M.R., Gupta V.K., Faridbod F., Norouzi P. Lanthanides Series Determination by Various Analytical Methods, Elsevier, Amsterdam Netherlands (2016), p. 47

[15] Coey J.M.D., Skumryev V., Gallagher K. Rare-earth metals: Is gadolinium really ferromagnetic

Natur, 401 (1999), pp. 35-36

[16] Roe W.C. Measurements of the magnetic anisotropy of gadolinium, Doctoral Thesis, Durham University, United Kingdom (1961), p. 4

[17] Nigh H.E., Legvold S., Spedding F.H. Magnetism and electrical resistivity of gadolinium single crystals. Phys. Review, 132 (3) (1963), pp. 1092-1097

[18] Aprea C., Maiorano A. A flexible numerical model to study an active magnetic refrigerator for near room temperature applications. Appl. Energy, 87 (2010), pp. 2690-2698

[19] Bru K., Christmann P., Labbé J.-F., Lefebvre G. Panorama 2014 du marché des Terres Rares

Rapport BRGM RP-65330-FR (2015)

[20] Rumbu R. Introduction à la métallurgie extractive des terres rares (third ed.), Roger Rumbu & Associates (2016)

[21] Kouzes R.T. The ^{3}He Supply Problem, Pacific Northwest National Laborator, PNNL-18388 (2009), pp. 1-12

[22] Wittenberg L.J. The Cost of Tritium Production in a Fusion Reactor, University of Wisconsin Fusion Technology Institute Report, UWFDM 871 (1991)

[23] Zsolnay D.M.M., Noy R.C., Nolthenius H.J., Trkov A. Summary description of the new International Reactor Dosimetry and Fusion File (IRDFF release 10), International Atomic Energy Agency, International Nuclear Data Committee, Vienna, Austria (2012)

[24] Carlson A.D., Pronyaev V.G., Smith D.L., Larson N.M., Chen Z., Hale G.M., Hambsch F.-J., Gai E.V., Oh S.-Y., Badikov S.A., Kawano T., Hofmann H.M., Vonach H., Tagesen S. I nternational evaluation of neutron cross section standards. Nucl. Data Sheets, 110 (12) (2009), pp. 3215-3324

[25] Kerkar N., Paulin P. Exploitation des coeurs REP, Collection Génie Atomique, Ed., EDP Sciences, Les Ulis, France (2008), pp. 6-9

[26] OE Fundamentals Handbook: Nuclear Physics and Reactor Theory, vol. 2, DOE-HDBK-1019/2-93, pp. 30-33 (1993).

[27] Bernard D., Santamarina A. Qualification of gadolinium burnable poison: Interpretation of MELUSINE/GEDEON-II spent fuel analysis. Ann. Nucl. Energy, 87 (Part 1) (2016), pp. 21-33

[28] T. Lian, D. Day, P. Hailey, J.-S. Choi, J. Farmer, Comparative study on the corrosion resistance of Fe-based amorphous metal, borated stainless steel and Ni-Cr-Mo-Gd alloy, Scientific Basis for Nuclear Waste Management XXX, Symposium NN, Boston, Massachussets, United Stated of America, 2006.

[29] J.-S. Choi, J.C. Farmer, C. Lee, L. Fischer, M. Boussoufi, B. Liu, H. Egbert, Neutron-Absorbing Coatings for Safe Storage of Fissile Materials with Enhanced Shielding and Criticality Safety, Materials Science & Technology Conference and Exhibition, Detroit, Michigan, United States of America (2007).

[30] Wilde E.W., Goli M.B., Berry C.J., Santo Domingo J.W., Martin H.L. Removal of gadolinium nitrate from heavy water, WSRC-TR-99-00096, Westinghouse Savannah River Company, Savannah River Site, Aiken, South Carolina, United States of America (2000)

[31] Pritychenko B., Běták E., Kellett M.A., Singh B., Totans J. The nuclear science references (NSR) database and web retrieval system. Nucl. Instrum. Methods Phys. Res. A, 640 (1) (2011), pp. 213-218

[32] Knoll G. Radiation Detection and Measurement (fourth ed.), Wiley & Sons Inc., New York (2010), pp. 519-520

[33] Sakurai Y., Kobayashi T. Experimental verification of the nuclear data of gadolinium for neutron capture therapy. J. Nucl. Sci. Technol., 39 (Sup. 2) (2002), pp. 1294-1297

[34] Enger S.A., Munck af Rosenschöld P., Rezaei A., Lundqvist H. Monte Carlo calculations of thermal neutron capture in gadolinium: A comparison of GEANT4 and MCNP with measurements. Med. Phys., 33 (2) (2006), pp. 337-341

[35] User's Manual Version 1.0. Pelowitz D.B. (Ed.), Los Alamos National Laboratory report, LA-CP-13-00364 (2013)

[36] Chadwick M.B., *et al.* Nuclear data for nuclear science and technology: Cross sections, covariances, fission product yields and decay data. Nucl. Data Sheets, 112, (12) (2011), pp. 2887-2996

[37] Y. Chen, Gadolinium neutron-capture gammas in Geant4, AARM Workshop 2015, Syracuse, Italia 2015.

[38] Roecker C. Geant4-Gd Shower Problem. ANNIE Collaboration 10/27, UC Berkeley, United States (2014)

[39] T. Yano, K. Hagiwara, I. Ou, P. Das, T. Mori, Y. Koshio, M. Sakuda, A. Kimura, H. Harada, N. Iwamoto, S. Nakamura, Measurement of gamma-ray production from thermal neutron capture on Gadolinium for neutrino experiments, VCI2016 –The 14th Vienna Conference on Instrumentation, Vienna, Austria (2016).

[40] Choi H.D., Firestone R.B., Lindstrom R.M., Molnr G.L.Please check author name, Mughabghab S.F., Paviotti-Corcuera R., *et al.* Database of prompt gamma rays from slow neutron capture for elemental analysis, International Atomic Energy Agency, Vienna (2007)

[41] Reich C.W. Nuclear Data Sheets for A = 156. Nucl. Data Sheets, 113 (11) (2012), pp. 2537-2840

[42] Helmer R.G. Nuclear Data Sheets for A = 158. Nucl. Data Sheets, 101 (3) (2004), pp. 325-519

[43] Gräfe J.L., McNeill F.E., Chettle D.R., Byun S.H. Characteristic X ray emission in gadolinium following neutron capture as an improved method of in vivo measurement: A comparison between feasibility experiment and Monte-Carlo simulation. Nucl. Instrum. Methods Phys. Res., 81 (2012), pp. 21-25

[44] Schultz D., Blasy B., Santana J.C., Young C., Petrosky J.C., McClory J.W., LaGraffe D., Brand J.I., Tang J., Wang W., Schemm N., Balkir S., Bauer M., Ketsman I., Fairchild R.W., Losovyj

Y.B., Dowben P.A. The K-shall Auger electron spectrum of gadolinium obtained using neutron capture in a solid state device. J. Phys. D: Appl. Phys., 43 (7) (2010), pp. 5502-5509

[45] Kandlakunta P. A Proof-of-Principle Investigation for a Neutron-Gamma Discrimination Technique in a Semiconductor Neutron Detector Thesis, Graduate School of the Ohio State University (2012), pp. 16-17

[46] Abdushukurov D.A. Gadolinium Foils as Converters of Thermal Neutrons, Nova Science Publishers Inc, New York, United States of America (2010), p. 14

[47] Kibédi T., Burrows T.W., Trzhaskovskaya M.B., Davidson P.M., Nestor Jr C.W. Evaluation of theoretical conversion coefficients using BrIcc. Nucl. Instrum. Methods Phys. Res. A, 589 (2008), pp. 202-229

[48] Rösel F., Fries H.M., Alder K., Pauli H.C. Internal conversion coefficients for all atomic shells. At. Data Nucl. Data Tables, 21 (1978), pp. 91-289

[49] Elam W.T., Ravel B.D., Sieber J.R. A new atomic database for X-ray spectroscopic calculations. Radiat. Phys. Chem., 63 (2) (2002), pp. 121-128

[50] Krause M.O. Atomic radiative and radiationless yields for K and L shells. J. Phys. Chem. Ref. Data, 8 (2) (2002), pp. 307-327

[51] Abdushukurov D.A. Gadolinium Foils as Converters of Thermal Neutrons, Nova Science Publishers, Inc., New York, United States of America (2010), pp. 34-41

[52] Jeavons A.P., Ford N.L., Linberg B., Sachot R. A new position-sensitive detector for thermal and epithermal neutrons. Nucl. Instrum. Methods, 148 (1) (1978), pp. 29-33

[53] Melchart G., Charpak G., Sauli F. The multistep avalanche chamber as a detector for thermal neutrons. Nucl. Instrum. Methods, 186 (3) (1981), pp. 613-630

[54] Abdushukurov D.A., Dzhuraev A.A., Evteeva S.S., Kovalenko P.P., Leskin V.A., Nikolaev V.A., Sirodzhi R.F., F.B Umarov. Model calculation of gadolinium-based converters of thermal neutrons. Nucl. Instrum. Methods Phys. Res., 84 (3) (1994), pp. 400-404

[55] Abdushukurov D.A., Abduvokhidov M.A., Bondarenko D.V., Muminov K.K., Toshov T.A., Chistyakov D.Y. Modeling the registration efficiency of thermal neutrons by gadolinium foils. J. Instrum., 2 (PO4001) (2007), pp. 1-13

[56] Masaoka S., Nakamura T., Yamagashi H., Soyama K. Optimization of micro-strip gas chamber as a two-dimensional neutron detector using gadolinium converter. Nucl. Instrum. Methods Phys. Res. A, 513 (2003), pp. 538-549

[57] Lee N.H., Kim S.H., Youk G.U., Park I.J., Kim Y.M. Development of a pMOSFET sensor with a Gd converter for low energy neutron dosimetry. Radiat. Prot. Dosim., 110 (1–4) (2004), pp. 277-281

[58] Lee N.H., Lee H.J., Hwang Y.G., Oh S.C., U.Youk G. Development of Gd-pMOSFET dosimeter for thermal neutron dosimetry. IEEE Trans. Nucl. Sci., 57 (6) (2010), pp. 3489-3492

[59] Vitale S.A., Gouker P.M. Gadolinium oxide coated fully depleted silicon-on-insulator transistors for thermal neutron dosimetry. Nucl. Instrum. Methods Phys. Res. A, 721 (2013), pp. 45-49

[60] McGregor D.S., Hammig M.D., Yang Y.-H., Gersch H.K., Klann R.T. Design considerations for thin film coated semiconductor thermal neutron detectors-I: Basics regarding alpha particle emitting neutron reactive films. Nucl. Instrum. Methods Phys. Res. A, 500 (1–3) (2003), pp. 272-308

[61] Blasy B.D. Neutron Detection Utilizing Gadolinium Doped Hafnium Oxide Films, Department of Engineering Physics Air Force Institute of Technology, Ohio, United States of America (2008)

[62] Fasasi M., Jung M., Siffert P., Teissier C. Thermal neutron dosimetry with cadmium telluride detectors. Radiat. Prot. Dosim., 23 (1988), pp. 429-431

[63] Miyake A., Nishioka T., Singh S., Morii H., Mimura H., Aoki T. A CdTe detector with a Gd converter for thermal neutron detection. Nucl. Instrum. Methods Phys. Res. A, 654 (2011), pp. 390-393

[64] ANSI N42.48-2008, American National Standard - Performance Requirements for Spectroscopic Personal Radiation Detectors (SPRDs) for Homeland Security (2008).

[65] Aoyama T., Oka Y., Honda K., Mori C. A neutron detector using silicon PIN photodiodes for personal neutron dosimetry. Nucl. Instrum. Methods Phys. Res. A, 314 (1992), pp. 590-594

[66] Dumazert J., Coulon R., Kondrasovs V., Boudergui K. Compensation scheme for online neutron detection using a gadolinium-covered CdZnTe sensor. Nucl. Instrum. Methods Phys. Res. A, 857 (2017), pp. 7-15

[67] Dumazert J., Coulon R., Bertrand G.H.V., Normand S., Méchin L., Hamel M. Compensated bismuth-loaded plastic scintillators for neutron detection using low-energy pseudo-spectroscopy. Nucl. Instrum. Methods Phys. Res. A, 819 (2016), pp. 25-32

[68] Kandlakunta P., Cao L.R., Mulligan P. Measurement of internal conversion from Gd neutron capture. Nucl. Instrum. Methods Phys. Res. A, 705 (2013), pp. 36-41

[69] Glodo J., Higgins W.M., van Loef E.V.D., Shah K.S. GdI_3:Ce - A new gamma and neutron scintillator. IEEE Nuclear Science Symposium Conference Record, 3 (2006), pp. 1574-1577

[70] Bertrand G.H.V., Hamel M., Normand S., Sguerra F. Pulse shape discrimination between (fast and thermal) neutrons and gamma rays with plastic scintillators: State of the art. Nucl. Instrum. Methods Phys. Res. A, 776 (2015), pp. 114-128

[71] Czirr J.B. Gd-loaded plastic scintillator. Nucl. Instrum. Methods, 108 (3) (1973), p. 613

[72] Brudanin V.B., Bregadze V.I., Gundorin N.A., Filossofov D.V., Kochetov O.I., Nemtchenok I.B., Smolnikov A.A., Vasiliev S.I. Element-loaded organic scintillators for neutron and neutrino physics. Part. Nuclei. Lett., 109 (6) (2001), pp. 69-77

[73] Nemchenok I.B., Gundorin N.A., Shevchik E.A., Shurenkova A.A. Plastic scintillators for thermal neutrons detection. Funct. Mater., 20 (3) (2013), pp. 310-314

[74] Velmozhnaya E.S., Bedrik A.I., Zhmurin P.N., Titskaya V.D., Adadurov A.F., Sofronov D.S. Investigation of the behavior of gadolinium complexes in plastic scintillation. Funct. Mater., 20 (4) (2013), pp. 494-499

[75] Watanabe M., Katsumata M., Ono H., Suzuki T., Miyata H., Itoh Y., Ishida K., Tamura M., Yamaguchi Y. First performance test of newly developed plastic scintillator for radiation detection. Nucl. Instrum. Methods Phys. Res. A, 770 (2015), pp. 197-202

[76] Bell Z.W., Brown G.M., Ho C.H., Sloop Jr F.V. Organic scintillators for neutron detection. X-ray and Gamma-Ray Detectors and Applications IV, Proceedings of SPIE, vol. 4784 (2002), pp. 150-163

[77] Ovechnika L., Riley K., Miller S., Bell Z., Nagarkar V. Gadolinium-loaded plastic scintillators for high-efficiency neutron detection. Phys. Procedia, 2 (2) (2009), pp. 161-170

[78] Bertrand G.H.V., Dumazert J., Sguerra F., Coulon R., Corre G., Hamel M. Understanding behavior of different metals in loaded scintillators: Discrepancy between gadolinium and bismuth. J. Mater. Chemi. C, 3 (2015), pp. 6006-6011

[79] Aberle C., Buck C., Gramlich B., Hartmann F.X., Lindner M., Schönert S., Schwan U., Wagner S., Watanabe H. Large scale Gd-beta-diketonate based organic liquid scintillator production for antineutrino detection. J. Instrum., 7 (2012), pp. 6008-6023

[80] Dumazert J., Coulon R., Hamel M., Carrel F., Sguerra F., Normand S., Méchin L., Bertrand G.H, V. Gadolinium-loaded plastic scintillators for thermal neutron detection using compensation. IEEE Trans. Nucl. Sci., 63 (3) (2016), pp. 1551-1564

[81] Cai W., Chen Q., Cherepy N., Dooraghi A., Kispaugh D., Chatziioannou A., Payne S., Wang W., Pei Q. Synthesis of bulk-size transparent gadolinium oxide-polymer nanocomposites for gamma ray spectroscopy. J. Mater. Chemi. C, 1 (2013), pp. 1970-1976

[82] Williams A.M., Beelev P.A., Spyrou N.M. Response of a lithium gadolinium borate scintillator in monoenergetic neutron fields. Radiat. Prot. Dosim., 110 (1–4) (2004), pp. 497-502

[83] Slaughter D.M., Stuart C.R., Klaas R.F., Merrill D.B. Performance of large neutron detectors containing lithium-gadolinium-borate scintillators. IEEE Trans. Nucl. Sci., 63 (3) (2016), pp. 1650-1658

[84] Medhat M.E., Wang Y. Estimation of background spectrum in a shielded HPGe detector using Monte Carlo simulations. Appl. Radiat. Isot., 84 (2014), pp. 13-18

[85] Hubbell J.H., Seltzer S.M. Tables of X-ray Mass Attenuation Coefficients and Mass Energy-Absorption Coefficients from 1 keV to 20 MeV for Elements Z = 1 to 92 and 48 Additional Substances of Dosimetric Interest, Radiation Physics Division, PML, NIST (1996)

[86] Beil H., Bergère R., Veyssière A. Détection de photoneutrons avec un scintillateur liquide chargé au gadolinium. Service de Physique Appliqué, 4 (2) (1969), pp. 249-250

[87] Beriguete W., Cao J., Ding Y., Hans S., Heeger K.M., Hu L., Huang A., Luk K.-B., Nemchenok I., Qi M., Rosero R., Sun H., Wang R., Wang Y., Wen L., Yang Y., Yeh M., Zhang Z., Zhou L. Production of a gadolinium-loaded liquid scintillator for the Daya Bay reactor neutrino experiment. Nucl. Instrum. Methods Phys. Res. A, 763 (2014), pp. 82-88

[88] Kim B.R., Han B., Jeon E., Joo K.K., Kim H.J., Kim H., Kim J., Ko Y., Lee J., Lee J., Lee M., Ma K., Oh Y., Park H., Park K., Seo K., Seon G.-W., Siyeon K. Development and mass production of a mixture of LAB- and DIN-based gadolinium-loaded liquid scintillator for the NEOS short-baseline neutrino experiment. J. Radioanal. Nucl. Chem., 310 (1) (2016), pp. 311-316

[89] Dazeley S., Bernstein A., Bowden N.S., Svoboda R. Observation of neutrons with a Gadolinium doped water Cherenkov detector. Nucl. Instrum. Methods Phys. Res. A, 607 (2009), pp. 616-619

[90] Dazeley S., Sweany M., Bernstein A. SNM detection with an optimized water Cherenkov neutron detector. Nucl. Instrum. Methods Phys. Res. A, 693 (2012), pp. 148-153

[91] Dazeley S., Ashgari A., Bernstein A., Bowden N.S., Mozin V. A water-based neutron detector as a multiplicity counter. Nucl. Instrum. Methods Phys. Res. A, 771 (2015), pp. 32-38

[92] A.P. Simpson, S. Jones, M.J. Clapham, S.A. McEhlaney, A review of neutron detection technology alternatives to helium-3 for safeguards applications, Institute of Nuclear Materials Management 52nd Annual Meeting (2011).

[93] G. Sannié, V. Kondrasov, G. Corre, K. Boudergui, B. Perot, Scintilla European project, the successful research results, 4th International Conference on Advancements in Nuclear Instrumentation Measurements Methods and their Applications (ANIMMA) 2015, Lisbon, Portugal (2015).

[94] W.J. Richard, Scintillator detector with gadolinium-based sidewall axial restraint and compliance assembly, Patent EP 1403661 A1, 2004.

[95] De Vita R., Ambi F., Battaglieri M., Osipenko M., Piombo D., Ricco G., Ripani M., Taiuti M. A large surface neutron and photon detector for civil security applications. Nucl. Instrum. Methods Phys. Res. A, 617 (1–3) (2010), pp. 219-222

[96] Fanchini E. Performance of an RPM Based on Gd-lined Plastic Scintillator for Neutron and Gamma Detection. IEEE Trans. Nucl. Sci., 33 (1) (2016), pp. 392-399

[97] ANSI N4242-2006, American National Standard — American National Standard Data Format Standard for Radiation Detectors Used for Homeland Security (2006).

[98] Pawełczak I.A., Tõke J., Henry E., Quinlan M., Singh H., W.U Schröder. NSTAR — A capture gated plastic neutron detector. Nucl. Instrum. Methods Phys. Res. A, 629 (2011), pp. 230-238

[99] Huber P. Detector of antineutrino spectra from nuclear reactors. Phys. Rev. C, 84 (024617) (2011), pp. 1-16

[100] Kuroda Y., Oguri S., Kato Y., Nakata R., Inoue Y., Ito C., Minowa M. A mobile antineutrino detector with plastic scintillators. Nucl. Instrum. Methods Phys. Res. A, 690 (2012), pp. 41-47

[101] Oguri S., Kuroda Y., Kato Y., Nakata R., Inoue Y., Ito C., Minowa M. Reactor antineutrino monitoring with a plastic scintillator array as a new safeguard. Nucl. Instrum. Methods Phys. Res. A, 757 (2014), pp. 33-39

[102] Dumazert J., Coulon R., Carrel F., Corre G., Normand S., Méchin L., Hamel M. Sensitive and transportable gadolinium-core plastic scintillator sphere for neutron detection and counting. Nucl. Instrum. Methods Phys. Res. A, 828 (2016), pp. 181-190

[103] Rühm W., Mares V., Pioch C., Agosteo S., Endo A., Ferrarini M., Rakhno I., Rollet S., Satoh D., Vincke H. Comparison of Bonner sphere responses calculated by different Monte Carlo codes at energies between 1 MeV and 1 GeV - Potential impact on neutron dosimetry at energies higher than 20 MeV. Radiat. Meas., 67 (2014), pp. 23-34

[104] J. Dumazert, R. Coulon, M. Hamel, G. Corre, F. Carrel, K. Boudergui, Gadosphere: A Gd-based plastic detector for wide spectrum neutron detection, 2nd International Conference on CBRNE – Research & Innovation, Lyon, France, 2017.

[105] Roecker C., Bernstein A., Bowden N.S., Cabrera-Palmer B., Dazeley S., Gerling M., Marleau P., Sweany M.D., Vetter K. Design of a transportable high efficiency fast neutron spectrometer. Nucl. Instrum. Methods Phys. Res. A, 826 (2016), pp. 21-30

[106] Bé M.-M., Chisté V. $^{252}_{98}Cf$, Table de radionucléides, LNE-LNHB/CEA (2007)

[107] International Commission on Radiological Protection 2007, The 2007 Recommendations of the International Commission on Radiological Protection, ICRP Publication 103 (2007).